TU Delft

Delft University of Technology

Circular representative volume elements for strain localization problems

Hofman, Pieter; Ke, Lu; van der Meer, Frans P.

DOI
10.1002/nme.7142

Publication date
2022

Document Version
Final published version

Published in
International Journal for Numerical Methods in Engineering

Citation (APA)
Hofman, P., Ke, L., & van der Meer, F. P. (2022). Circular representative volume elements for strain localization problems. *International Journal for Numerical Methods in Engineering*, *124*(4), 784-807. https://doi.org/10.1002/nme.7142

Important note
To cite this publication, please use the final published version (if applicable).
Please check the document version above.

Copyright
Other than for strictly personal use, it is not permitted to download, forward or distribute the text or part of it, without the consent of the author(s) and/or copyright holder(s), unless the work is under an open content license such as Creative Commons.

Takedown policy
Please contact us and provide details if you believe this document breaches copyrights.
We will remove access to the work immediately and investigate your claim.

This work is downloaded from Delft University of Technology.
For technical reasons the number of authors shown on this cover page is limited to a maximum of 10.

Check for updates

Received: 30 November 2021 | Accepted: 2 September 2022

DOI: 10.1002/nme.7142

RESEARCH ARTICLE

WILEY

Circular representative volume elements for strain localization problems

Pieter Hofman | **Lu Ke** | **Frans P. van der Meer**

Faculty of Civil Engineering and Geosciences, Delft University of Technology, Delft, The Netherlands

Correspondence
Pieter Hofman, Faculty of Civil Engineering and Geosciences, Delft University of Technology, 2600 GA Delft, The Netherlands.
Email: p.hofman@tudelft.nl

Funding information
Dutch Research Council NWO, Vidi grant, Grant/Award Number: 16464

Abstract

A common choice for multiscale modeling of the mechanical response of composites is to use periodic boundary conditions (PBCs) on square and cubical representative volume elements (RVEs). However, when strain localization occurs in the micromodel, these PBCs are unable to reproduce the transverse isotropy of composite materials with a random microstructure. Existing remedies to alleviate this issue have been proposed in literature by either rotating or shifting the periodicity constraints. However, this results in a mismatch of the microstructure on opposing edges which may prevent cracks to cross the boundary and consequently limit the supported localization angles. Furthermore, in absence of a strategy that ensures a single localization band to arise in a fracturing RVE, it is difficult to formulate a generic expression for the length scale parameter that is used to regulate the energy dissipation, which plays an important role in obtaining RVE-size objective results. As an alternative to square (or cubical) RVEs, circular (or spherical) RVEs have been proposed in literature since they provide a response which is independent of the orientation due to shape of the RVE. However, it is shown in this work that the existing formulation with straightforward application of PBCs on a circular RVE fails to predict the correct softening behavior, due to over-constraining when cracks reach the boundary. Therefore, a new formulation of PBCs on a circular RVE is proposed, which allows for a single fully developed localization band under arbitrary angle. The performance of the new formulation is tested with a series of simulations where macroscopic strains are imposed under varying orientations. It is demonstrated that the circular RVE with the new formulation of PBCs successfully predicts a transversely isotropic response with full softening without the issue of mismatching microstructure as with previously developed remedies for the square RVE. In addition, it is shown that the length scale parameter is well-defined and independent of the orientation of the circular RVE.

KEYWORDS

composite materials, multiscale modeling, periodic boundary conditions, representative volume elements, strain localization, transverse isotropy

This is an open access article under the terms of the Creative Commons Attribution License, which permits use, distribution and reproduction in any medium, provided the original work is properly cited.
© 2022 The Authors. *International Journal for Numerical Methods in Engineering* published by John Wiley & Sons Ltd.

10970207, 0, Downloaded from https://onlinelibrary.wiley.com/doi/10.1002/nme.7142 by Tu Delft, Wiley Online Library on [22/11/2022]. See the Terms and Conditions (https://onlinelibrary.wiley.com/terms-and-conditions) on Wiley Online Library for rules of use; OA articles are governed by the applicable Creative Commons License

1 | INTRODUCTION

Composites are materials that consist of two or more phases with different physical behavior. The overall effective properties of a composite material depend on the microstructural geometry, the material properties of the individual phases and the bonding between the constituents. When loading these composites, microcracks grow and coalesce and a macroscopic crack develops, which may lead to structural failure at the larger scale. The failure process in composite materials is therefore an intrinsically multiscale phenomenon.

In order to tailor the microstructure of the material to obtain desired characteristics or to verify its safety when it is used in structural applications, tests need to be performed for assessing the mechanical response of the material when subjected to load and environmental conditions. For composite materials with a complex microstructure and a response that is highly nonlinear and history dependent, it is often intractable to formulate macroscopic phenomenological constitutive relations that are accurate for all relevant scenarios based on physical experiments performed on the macroscale.[1] However, obtaining accurate phenomenological constitutive relations of the individual constituents is in most cases more practical. In order to take into account the microstructural processes and to circumvent any restrictive assumptions on the material behavior at the higher scales, multiscale computational methods have been developed. In these approaches, a macroscopic material point is coupled with a micromodel in which the heterogeneities, with the corresponding constitutive relations for the individual constituents, are modeled in detail. Simulations are then performed simultaneously on both scales while information is exchanged in between, thereby replacing macroscopic material models.

The micromodel should accurately represent the microstructure, that is, it should have enough constituents with the correct physical characteristics and the response must resemble the overall effective behavior of the material. In addition, the coupling between the macro and the micro model must be well-defined. In computational homogenization the macroscopic kinematics are transferred to the micromodel in the form of appropriate boundary conditions (BCs). After solving the micro boundary value problem (BVP), a homogenization procedure is performed to determine the macroscopic stress, traction and associated tangents.

A common way of imposing the macroscopic kinematics is with periodic boundary conditions (PBCs) on cubical (or square in 2D) representative volume elements (RVEs). However, due to the shape of the square RVE and the consequently orthogonal periodicity directions, these PBCs only support localization patterns comprising bands that cross the boundary on opposing points. The response of the square RVE with PBCs therefore depends on the orientation of the RVE with respect to the loading and consequently fails to predict the *isotropic* (in a statistical sense) response that is characteristic of composite materials with a random microstructure.

In literature, several remedies have been proposed to allow for inclined localization bands in square or cubical RVEs.[2-4] These approaches are based on aligning the periodic constraints with (developing) localization bands. This is either done by applying a shift or a rotation to the function that couples opposing points. However, with RVEs representing random microstructures where stiff inclusions or fibers are allowed to exist on the boundary, it has been shown that this results in a mixed coupling of points that correspond to inclusions and matrix, leading to an artificial reinforcement along the RVE boundary and possibly preventing RVE-wide crack bands to cross the edges.[5] Moreover, either a priori knowledge of the localization angle is required or the BCs need to be updated during the analysis which may harm robustness by causing abrupt changes in the RVE deformation, as reported by Coenen et al.[4] and remedied in the same work by introducing additional external forces to the coupled nodes in order to maintain equilibrium from one time step to the other. Finally, the crack length differs when the orientation of the square RVE or the loading changes, which affects the homogenized energy dissipation. In some approaches, this last issue can be corrected by introducing a length scale parameter that smears the macroscopic jump over the RVE in order to obtain RVE size objective results and to conserve energy equivalence between the scales.[6-10] However, it is not proven that this length scale parameter can be obtained in all cases. In particular when complex crack patterns occur, this parameter is not well defined.[11] Therefore, the formulation of appropriate BCs for obtaining a transversely isotropic response in strain localization problems is still an unresolved issue.

To resolve the issues of a mismatch of fibers along the RVE boundary and the dependence of the length scale parameter on the orientation of the cubical RVE, we explore a spherical (or circular in 2D) shape for the RVE in this article.

Spherical RVEs with PBCs have been proposed by Glüge et al.[12] and provide a promising alternative, since the micromodel is intrinsically orientation independent due to its shape.* However, the effectiveness of the BCs in representing complete failure of the material has not been demonstrated. It is shown in this work that the existing formulation of periodicity on a (two-dimensional) circular RVE is not able to provide a full softening response. Therefore, a new formulation of PBCs on a circular RVE, which allows for fully localized deformations and arbitrarily inclined localization angles, is proposed in this article.

10970207, 0, Downloaded from https://onlinelibrary.wiley.com/doi/10.1002/nme.7142 by Tu Delft, Wiley Online Library on [22/11/2022]. See the Terms and Conditions (https://onlinelibrary.wiley.com/terms-and-conditions) on Wiley Online Library for rules of use; OA articles are governed by the applicable Creative Commons License

The outline of this article is as follows: First the multiscale framework for strain localization problems, for which the circular micromodel provides an alternative to the square micromodel, is discussed in Section 2. After that, the existing three-dimensional formulation of PBCs on a spherical RVE by Glüge et al.[12] is studied in a two-dimensional setting with circular RVEs in Section 3, and it is argued that the existing formulation is not suitable for studying localization problems. Therefore, a new formulation of PBCs on a circular RVE is proposed in Section 4. The new formulation is tested and the response is compared to the square RVE with classical PBCs with several numerical examples in Section 5. Finally, the conclusions are presented in Section 6.

Throughout this article, superscripts M denote quantities with respect to the macroscale, while microscale quantities have no superscripts. Furthermore, tensor notation is used where bold-faced letters denote tensors and vectors.

2 | MULTISCALE FRAMEWORK FOR STRAIN LOCALIZATION PROBLEMS

Classical first order computational homogenization is based on the assumption of a strict separation of scales, where the macroscopic strain field is assumed to be constant over the volume occupied by the RVE and where the RVE is sufficiently large such that the response is statistically representative for the material.[13] With this method, each macroscopic material point is attached to a micromodel. In the strain-driven approach, a macroscopic strain is imposed on the micromodel via the BCs. After solving the microscale BVP, the macroscopic stress (defined as the volume average of the microscopic stress) is computed, together with the tangent operator, and passed to the macroscopic material point.

When localization of deformation occurs, the classical assumption of a strict separation of scales, is violated and the micromodel cannot be considered to be statistically representative for the surrounding material anymore (only in the direction along the crack). As a consequence, the stress-strain response loses objectivity with respect to the RVE size:[14] when the RVE size is increased, the homogenized stress-strain response becomes more brittle since the energy dissipation in the localization band does not scale proportionally with the RVE size. Moreover, the macroscopic BVP becomes ill-posed and suffers from pathological mesh-size dependency.

To overcome these issues, discontinuous schemes have been developed where a discontinuity, for example, with XFEM or zero-thickness interface elements, is inserted at the macroscale as soon as a certain failure criterion, based on the homogenized quantities,[15,16] is reached. In these approaches, the homogenized relation is a traction–separation relation instead of a stress-strain relation. Prior to localization, the macroscopic constitutive relation is linear elastic and comes from *offline* homogenization of the microscale response. From the onset of localization, the discontinuous homogenization scheme is adopted with nested micro BVP computations, to compute the macroscopic tractions. However, this approach is only accurate when the nonlinear response prior to localization is negligible.[17]

The drawbacks from the discontinuous schemes can be resolved by the introduction of a continuous-discontinuous approach in which the complex loading histories and strong nonlinearities prior to localization are taken into account. Nguyen presented a method where an RVE, which is attached to a bulk integration point, is cloned after localization is detected and subsequently a crack is inserted at the macroscale.[17] The RVE is then attached to the macro crack integration point, while the other bulk integration points are assumed to unload elastically. The homogenized response comes from averaging in a failure zone to ensure RVE size independence and is therefore mainly applicable with a continuum damage model (CDM) on the microscale.

More recently, several continuous-discontinuous schemes have been developed[6-10] which do not require any assumptions on the material models at the microscale. In the approach proposed by Oliver et al.,[6] the first order classical computational homogenization framework transitions into a homogenization framework for the strain localization case with minimal changes to the procedure: The downscaled macroscopic strain is replaced by an *equivalent* macroscopic strain that consists of a bulk strain and volume averaged jump term, defined as

$$\boldsymbol{\mathcal{E}}^M \equiv \boldsymbol{\varepsilon}_b^M + \frac{1}{h}[\![\boldsymbol{u}^M]\!] \otimes^s \boldsymbol{n}_\Gamma^M, \tag{1}$$

where $\otimes$ denotes the tensor product and superscript s represents the symmetric part of the tensor, $\boldsymbol{\varepsilon}_b^M$ is the macroscopic bulk strain and $[\![\boldsymbol{u}^M]\!]$ is the macroscopic jump defined as $[\![\boldsymbol{u}^M]\!] \equiv \left(\boldsymbol{u}^M\right)^+ - \left(\boldsymbol{u}^M\right)^-$, where the + and − signs denote the macroscopic displacement on the positive and negative side of the crack, respectively. Note that the averaging of the jump term requires a length scale parameter h that takes into account the micromodel size and plays an important role in removing the pathological dependence of the response on the RVE size by ensuring that energy transfer is consistent between

10970207, 0, Downloaded from https://onlinelibrary.wiley.com/doi/10.1002/nme.7142 by Tu Delft, Wiley Online Library on [22/11/2022]. See the Terms and Conditions (https://onlinelibrary.wiley.com/terms-and-conditions) on Wiley Online Library for rules of use; OA articles are governed by the applicable Creative Commons License

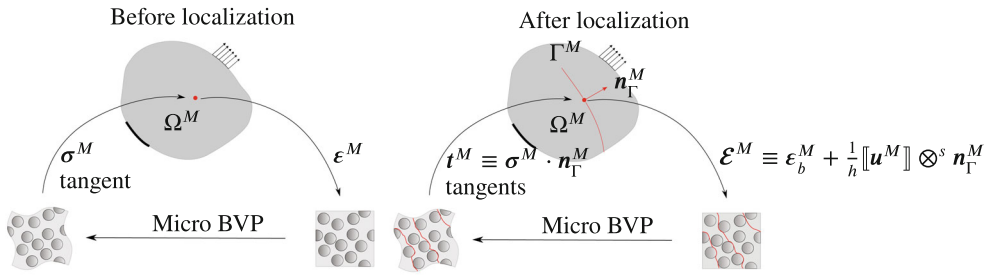

FIGURE 1 Multiscale framework. Left: Classical first order computational homogenization. Right: Computational homogenization for strain localization. After localization is detected, the macroscopic strain $\boldsymbol{\varepsilon}^M$ is replaced by the *equivalent* macroscopic strain $\boldsymbol{\mathcal{E}}^M$ and the homogenization framework transitions from a stress–strain relation to a traction–separation relation.

scales. The traction–separation relations are obtained from the homogenization of the nested micro BVPs, together with tangent operators for the cohesive integration points. The traction is obtained with the Cauchy stress theorem from the homogenized stress, which is the volume averaged microscopic stress. An overview of the flow of actions before and after the onset of localization is given in Figure 1.

The focus in this article is on the micromodel and the application of appropriate BCs in the case of strain localization. Therefore, single scale analyses of the micromodel are considered where the *equivalent* macroscopic strain $\boldsymbol{\mathcal{E}}^M$ is provided as an input and the computed output is the macroscopic stress $\boldsymbol{\sigma}^M$. The well-known loss of RVE-size objectivity with respect to the homogenized softening stress-strain response in the case of strain localization,[14] is acknowledged with the remark that computing homogenized stress from macroscopic strain is an essential part of formulations in which objectivity of the macroscale response is restored.

3 | EXISTING FORMULATION OF PERIODIC BOUNDARY CONDITIONS ON A CIRCULAR RVE

Instead of using cubical RVEs, Glüge et al.[12,18] discussed the applicability of spherical RVEs since they are intrinsically orientation independent because of their shape. In order to apply PBCs such that the kinematics and energy dissipation are consistent between the scales, it is required that coupled points have anti-periodic normals ($\boldsymbol{n}^+ = -\boldsymbol{n}^-$), such that the contribution of the microfluctuation to the microscopic average strain and average stress power vanishes.[12] The macroscopic strain is then imposed on the micromodel via the following master-slave constraint equation that couples the displacements $\{\boldsymbol{u}^+, \boldsymbol{u}^-\}$ of opposite points to each other

$$\boldsymbol{u}^+ = \boldsymbol{u}^- + \boldsymbol{\varepsilon}^M \cdot (\boldsymbol{x}^+ - \boldsymbol{x}^-), \quad \boldsymbol{x} \in \partial\Omega^+, \tag{2}$$

where the external boundary can be arbitrarily split in two halves such that $\partial\Omega^+ \cup \partial\Omega^- = \partial\Omega$ and $\partial\Omega^+ \cap \partial\Omega^- = \emptyset$. Also note that the macroscopic strain $\boldsymbol{\varepsilon}^M$ transitions to the *equivalent* macroscopic strain $\boldsymbol{\mathcal{E}}^M$ after localization is detected (as described in Section 2). A schematic of the application of Equation (2) on a two-dimensional circular RVE with domain Ω and external boundary $\partial\Omega$ is shown in Figure 2. It should be noted that the macroscopic strain must be imposed directly on each pair of nodes. It is not possible to use control (corner) nodes as commonly performed with the square RVE, since the relative coordinate vector connecting opposing nodes is different for each pair, which results in the inability of expressing the inhomogeneous side of the constraint equations in terms of control displacements. In order to prevent rigid body translations, one node is fixed.

In the following section, it will be demonstrated with an analytical example that these BCs (Equation 2) do not allow for a complete separation in two unloaded hemicircles, thereby preventing a realistic softening response.

3.1 | Analytical example

Let us consider the case where a horizontal uniaxial strain is imposed on a circular micromodel via Equation (2). The components with respect to a Cartesian basis $\{\boldsymbol{e}_x, \boldsymbol{e}_y\}$, are prescribed as $\varepsilon_{xx}^M \neq 0$, $\varepsilon_{xy}^M = \varepsilon_{yx}^M = 0$, $\varepsilon_{yy}^M = 0$. With a material

10970207, 0, Downloaded from https://onlinelibrary.wiley.com/doi/10.1002/nme.7142 by Tu Delft, Wiley Online Library on [22/11/2022]. See the Terms and Conditions (https://onlinelibrary.wiley.com/terms-and-conditions) on Wiley Online Library for rules of use; OA articles are governed by the applicable Creative Commons License

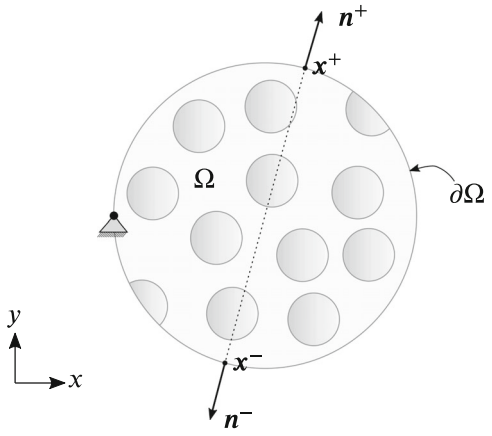

FIGURE 2 Schematic of the circular RVE with PBCs. Displacements of points with opposing normals are coupled to each other via Equation (2).

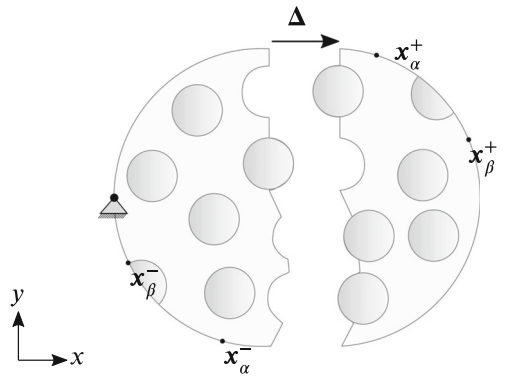

FIGURE 3 Preferred ultimate failure mode with the circular RVE

model that favors mode-I (opening) failure, monotonically increasing the macroscopic strain results in a full crack that is perpendicular to the load direction. After localization is detected, the macroscopic strain is replaced by the *equivalent* macroscopic strain (as explained in Section 2). Since the jump is in the same direction as the normal of the crack, the components of the *equivalent* macroscopic strain are $\mathcal{E}^M_{xx} \neq 0,\ \mathcal{E}^M_{xy} = \mathcal{E}^M_{yx} = 0,\ \mathcal{E}^M_{yy} = 0$.

The (desired) final failure mode, with a fully developed crack and two unloaded hemicircles, is shown in Figure 3. The application of the PBCs on two arbitrary node pairs $\{\boldsymbol{x}^-_\alpha, \boldsymbol{x}^+_\alpha\}$ and $\{\boldsymbol{x}^-_\beta, \boldsymbol{x}^+_\beta\}$ in x-direction leads to

$$u^+_{\alpha x} - u^-_{\alpha x} = \mathcal{E}^M_{xx}\left(x^+_\alpha - x^-_\alpha\right), \tag{3}$$

$$u^+_{\beta x} - u^-_{\beta x} = \mathcal{E}^M_{xx}\left(x^+_\beta - x^-_\beta\right). \tag{4}$$

From the figure, it can be observed that the preferred ultimate failure mode corresponds to $u^+_{\alpha x} = \Delta$, $u^+_{\beta x} = \Delta$ and $u^-_{\alpha x} = 0$, $u^+_{\beta x} = 0$. Substituting these in Equation (2) for both node pairs yields

$$\Delta = \mathcal{E}^M_{xx}\left(x^+_\alpha - x^-_\alpha\right), \tag{5}$$

$$\Delta = \mathcal{E}^M_{xx}\left(x^+_\beta - x^-_\beta\right). \tag{6}$$

10970207, 0, Downloaded from https://onlinelibrary.wiley.com/doi/10.1002/nme.7142 by Tu Delft, Wiley Online Library on [22/11/2022]. See the Terms and Conditions (https://onlinelibrary.wiley.com/terms-and-conditions) on Wiley Online Library for rules of use; OA articles are governed by the applicable Creative Commons License

However, since $x_\alpha^+ - x_\alpha^- \neq x_\beta^+ - x_\beta^-$, there exists no value for $\mathcal{E}_{xx}^M$ for which Equations (5) and (6) are both satisfied with $\Delta \neq 0$. Therefore, a deformation mode that corresponds to complete separation in two parts of the RVE is not supported by the imposed constraint equation (Equation 2) and consequently a realistic softening response is prevented.

The consequence of this will be demonstrated in the numerical examples in Section 5, but first an alternative formulation is presented in the next section that does support the deformation from Figure 3. Finally we remark that, although PBCs for square RVEs can also be described with Equation (2), square RVEs do not suffer from the same problem because node pairs are defined horizontally and vertically rather than diagonally such that the relative coordinate vectors $(\boldsymbol{x}^+ - \boldsymbol{x}^-)$ are the same for all node pairs along a whole edge. In other words, when the horizontal and vertical edges of the square RVE are aligned with the x- and y-coordinates, respectively, with loading in x-direction as in Figure 3, both nodes of any node pair on the opposing horizontal edges will be on the same side of the vertical crack.

4 | NEW FORMULATION OF PERIODIC BOUNDARY CONDITIONS ON A CIRCULAR RVE

It has been demonstrated in the previous section that the existing formulation of PBCs imposed on the boundary of a circular RVE does not support a final deformation mode with a separation in two halves. The analytical example showed that the origin of the over-constraining is directly related to the inhomogeneous part in the constraint equations (Equation 2). Since a nonzero *equivalent* macroscopic strain is imposed, the inhomogeneous part scales with the distance vector between the nodes. However, when localization of deformation occurs in the RVE, this becomes problematic. In the final state of the RVE, a jump is required between nodes that are opposite to each other, which cannot be achieved with the existing formulation of PBCs on the circular RVE boundary.

In order to transition from the existing formulation of PBCs (Equation 2) before localization to a constraint equation that supports a fully failed state, we propose to add an *unknown* jump $[\![\hat{\boldsymbol{u}}]\!]$ to the existing formulation, which is defined as the relative displacement of two nodes $\{\hat{\boldsymbol{x}}^+, \hat{\boldsymbol{x}}^-\}$ that are on either side of where the discontinuity crosses the edge (see Figure 4). In order to allow for the bulk material to elastically unload while the jump $[\![\hat{\boldsymbol{u}}]\!]$ increases, it is required to reduce the strain term in Equation (2) with a *correction* term defined as

$$\hat{\boldsymbol{\varepsilon}} \equiv \frac{1}{\gamma} [\![\hat{\boldsymbol{u}}]\!] \otimes^s \boldsymbol{n}_\Gamma^M, \tag{7}$$

where the normal $\boldsymbol{n}_\Gamma^M$ is the macroscopic crack normal that is determined when localization is detected (e.g., with the acoustic tensor based on the macroscopic quantities). Note that γ is a length scale parameter which is required such that $\hat{\boldsymbol{\varepsilon}}$ is dimensionless. The definition of γ is determined in Section 4.1.

Performing the steps as described above, that is, reducing the *equivalent* macroscopic strain by the *correction* term $\hat{\boldsymbol{\varepsilon}}$ and adding the *unknown* jump $[\![\hat{\boldsymbol{u}}]\!]$ to Equation (2), we obtain the newly proposed PBCs

$$\boldsymbol{u}^+ = \boldsymbol{u}^- + (\boldsymbol{\mathcal{E}}^M - \hat{\boldsymbol{\varepsilon}}) \cdot (\boldsymbol{x}^+ - \boldsymbol{x}^-) + [\![\hat{\boldsymbol{u}}]\!], \quad \boldsymbol{x} \in \partial\Omega^+, \tag{8}$$

where the external boundary is split in two halves such that $\partial\Omega^+$ and $\partial\Omega^-$ are the parts of the boundary on the positive side and on the negative side of the discontinuity, respectively (see Figure 4). Note that prior to localization, the *unknown* microjump in Equation (8) is zero and the formulation reduces to the existing formulation of PBCs (Equation 2). After localization and when the RVE is fully failed, the constraint equations allow for a solution where $\boldsymbol{u}^+ = \boldsymbol{u}^- + [\![\hat{\boldsymbol{u}}]\!]$, with a constant jump and an undeformed bulk which is the required final deformation mode that was prevented with the original formulation (see Section 3.1). In the transition between onset of localization and the fully localized state, the microscopic jump may vary along the crack inside the RVE domain while the bulk material away from the crack is still stressed.

Furthermore, the jump and normal vector can, depending on the material, point in different directions (e.g., in orthogonal directions, representing mode-II (sliding) failure). The selection of the node pair $\{\hat{\boldsymbol{x}}^+, \hat{\boldsymbol{x}}^-\}$ can be determined when the orientation of the macroscopic crack is known. With the selection of the node pair and the proposed BCs, the microscopic crack will cross the boundary on opposing points. Consequently, as it is shown at the end of the next paragraph, the effective crack is a straight crack through the center of the specimen. Therefore, once the orientation of the macroscopic crack is known, the location where the microscopic crack should cross the boundary of the RVE is known, from which the selection of the node-pair automatically follows.

10970207, 0, Downloaded from https://onlinelibrary.wiley.com/doi/10.1002/nme.7142 by Tu Delft, Wiley Online Library on [22/11/2022]. See the Terms and Conditions (https://onlinelibrary.wiley.com/terms-and-conditions) on Wiley Online Library for rules of use; OA articles are governed by the applicable Creative Commons License

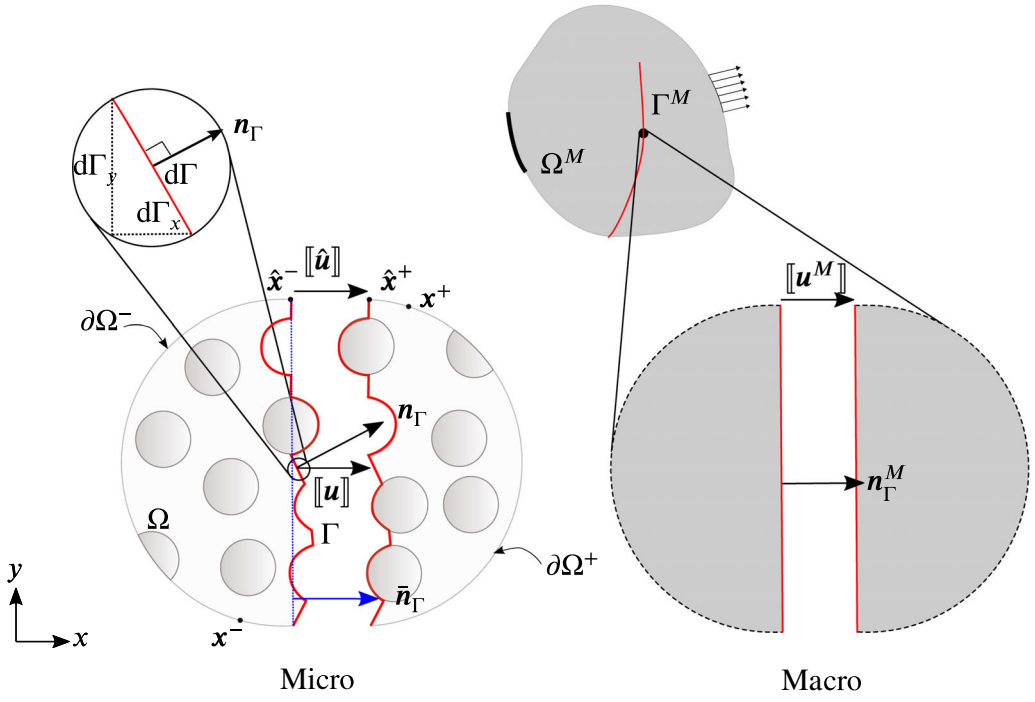

FIGURE 4 Microscopic (left) and macroscopic (right) final deformation mode. At the micro scale, the displacement can fluctuate and the crack can be tortuous.

In addition, it is emphasized that the new constraint equation, where the *unknown* jump $[\![\hat{\boldsymbol{u}}]\!]$ is a linear combination of the displacements of the node pair $\{\hat{\boldsymbol{x}}^+, \hat{\boldsymbol{x}}^-\}$, can still be enforced on the circular boundary as a master-slave constraint. In Equation (8), $\boldsymbol{u}^+$ contains slave degrees of freedom and $\{\boldsymbol{u}^-, \hat{\boldsymbol{u}}^+, \hat{\boldsymbol{u}}^-\}$ is the set of vectors that contains the master degrees of freedom.

4.1 | Condition of average strain consistency between scales

Let us consider the limit case where the RVE is in a fully failed state, that is, the localization band inside the RVE is fully developed and both parts on either side of the crack are elastically unloaded (see Figure 4). This deformation mode, which corresponds to a constant relative displacement between the nodes of a node pair, is supported by Equation (8) when the term inside the brackets on the right-hand side is zero ($\boldsymbol{\mathcal{E}}^M - \hat{\boldsymbol{\varepsilon}} = 0$). Thus, in this fully failed state, the following relation holds between the *unknown* microscopic jump and the imposed *equivalent* macroscopic strain

$$\frac{1}{\gamma}[\![\hat{\boldsymbol{u}}]\!] \otimes^s \boldsymbol{n}_\Gamma^M = \boldsymbol{\mathcal{E}}^M. \tag{9}$$

In order to satisfy the requirement of average strain consistency on both scales, the macroscopic *equivalent* strain should be equal to the (volume) averaged microscopic strain

$$\boldsymbol{\mathcal{E}}^M = \langle \boldsymbol{\varepsilon} \rangle_\Omega, \tag{10}$$

where $\langle \cdot \rangle_\Omega \equiv \frac{1}{|\Omega|}\int_\Omega (\cdot)\, \mathrm{d}\Omega$. In the fully failed state, the bulk strain is zero, while the jump is constant along the crack path Γ. The volume average of the corresponding (discontinuous) microscopic strain field is then

$$\langle \boldsymbol{\varepsilon} \rangle_\Omega = \langle \delta_\Gamma [\![\hat{\boldsymbol{u}}]\!] \otimes^s \boldsymbol{n}_\Gamma \rangle_\Omega, \tag{11}$$

10970207, 0, Downloaded from https://onlinelibrary.wiley.com/doi/10.1002/nme.7142 by Tu Delft, Wiley Online Library on [22/11/2022]. See the Terms and Conditions (https://onlinelibrary.wiley.com/terms-and-conditions) on Wiley Online Library for rules of use; OA articles are governed by the applicable Creative Commons License

where δ_Γ is a Dirac delta function, active at the discontinuity Γ. Subsequently, Equation (11) can be further evaluated as

$$\langle \boldsymbol{\varepsilon} \rangle_\Omega = \frac{1}{|\Omega|} \int_\Omega \delta_\Gamma \, [\![\hat{\boldsymbol{u}}]\!] \otimes^s \boldsymbol{n}_\Gamma \mathrm{d}\Omega = \frac{1}{|\Omega|} \int_\Gamma [\![\hat{\boldsymbol{u}}]\!] \otimes^s \boldsymbol{n}_\Gamma \mathrm{d}\Omega = \frac{1}{|\Omega|} [\![\hat{\boldsymbol{u}}]\!] \otimes^s \int_\Gamma \boldsymbol{n}_\Gamma \mathrm{d}\Gamma, \tag{12}$$

where the Dirac property is used to transform a volume integral to a surface integral. From Figure 4, it follows that $\frac{n_{\Gamma_x}}{|\boldsymbol{n}_\Gamma|} = \frac{\mathrm{d}\Gamma_y}{\mathrm{d}\Gamma} \rightarrow n_{\Gamma_x} \mathrm{d}\Gamma = \mathrm{d}\Gamma_y$ and similarly $n_{\Gamma_y} \mathrm{d}\Gamma = \mathrm{d}\Gamma_x$. Since the microscopic crack is enforced to cross the boundary at opposing points, the crack path is such that the distance traveled along the projected crack plane is equal to two times the radius of the RVE and in perpendicular direction it is equal to zero (for a crack aligned with the y-axis: $\int_{\Gamma_y} \mathrm{d}\Gamma_y = 2\mathrm{R}$ and $\int_{\Gamma_x} \mathrm{d}\Gamma_x = 0$). Thus, the surface integral of the microscopic normal along the crack path Γ in the last term in Equation (12) can be further elaborated as

$$\int_\Gamma \boldsymbol{n}_\Gamma \mathrm{d}\Gamma = \begin{bmatrix} \int_\Gamma n_{\Gamma_x} \mathrm{d}\Gamma \\ \int_\Gamma n_{\Gamma_y} \mathrm{d}\Gamma \end{bmatrix} = \begin{bmatrix} \int_{\Gamma_y} \mathrm{d}\Gamma_y \\ \int_{\Gamma_x} \mathrm{d}\Gamma_x \end{bmatrix} = 2\mathrm{R}\overline{\boldsymbol{n}}_\Gamma, \tag{13}$$

where the normal $\overline{\boldsymbol{n}}_\Gamma$ is the average normal vector along the microscopic crack Γ. Substituting the result of Equation (13) in Equation (12) yields the expression for the (volume) averaged microscopic strain field

$$\langle \boldsymbol{\varepsilon} \rangle_\Omega = \frac{2\mathrm{R}}{|\Omega|} [\![\hat{\boldsymbol{u}}]\!] \otimes^s \overline{\boldsymbol{n}}_\Gamma. \tag{14}$$

Substituting Equations (9) and (14) in the condition of average strain consistency (Equation 10) yields

$$\frac{1}{\gamma} [\![\hat{\boldsymbol{u}}]\!] \otimes^s \boldsymbol{n}_\Gamma^M = \frac{2\mathrm{R}}{|\Omega|} [\![\hat{\boldsymbol{u}}]\!] \otimes^s \overline{\boldsymbol{n}}_\Gamma. \tag{15}$$

In the implementation of these BCs (Equation 8), it is assumed that the final dominant crack always crosses the RVE boundary on the matrix phase. If the macroscopic crack normal $\boldsymbol{n}_\Gamma^M$ implies that the microscopic crack Γ should cross the boundary where an inclusion exists, then the normal $\overline{\boldsymbol{n}}_\Gamma$ is adjusted by choosing the node pair $\{\hat{\boldsymbol{x}}^+, \hat{\boldsymbol{x}}^-\}$ such that the crack crosses the boundary at the nearest point corresponding to matrix material. In this special case, $\boldsymbol{n}_\Gamma^M$ and $\overline{\boldsymbol{n}}_\Gamma$ do not coincide exactly which results in a slight mixed-mode deformation and consequently the microscopic volume average $\langle \boldsymbol{\varepsilon} \rangle_\Omega$ is slightly different from the macroscopic imposed strain $\boldsymbol{\mathcal{E}}^M$. However, with increasing RVE sizes, the difference between $\boldsymbol{n}_\Gamma^M$ and $\overline{\boldsymbol{n}}_\Gamma$ vanishes. Therefore, for a sufficiently large RVE, it follows from Equation (15) that the length scale parameter γ is defined as

$$\gamma \equiv \frac{|\Omega|}{2\mathrm{R}}, \tag{16}$$

which is the ratio of the volume over the effective crack length and can be recognized to be the same definition for the length-scale parameter as previously proposed in Reference 7.

4.1.1 | Definition of the macroscopic equivalent strain on a circular RVE

Note that in our work the *equivalent* macroscopic strain is provided as a single input in the constraint equations (see Section 2). However, in a strain-driven multiscale framework for strain localization, it is defined with the kinematic quantities on the macroscale (Equation 1).

Since the bulk strain is zero in the final deformation mode, it follows from Equations (1) and (9) that

$$\frac{1}{\gamma} [\![\hat{\boldsymbol{u}}]\!] \otimes^s \boldsymbol{n}_\Gamma^M = \frac{1}{h} [\![\boldsymbol{u}^M]\!] \otimes^s \boldsymbol{n}_\Gamma^M. \tag{17}$$

10970207, 0, Downloaded from https://onlinelibrary.wiley.com/doi/10.1002/nme.7142 by Tu Delft, Wiley Online Library on [22/11/2022]. See the Terms and Conditions (https://onlinelibrary.wiley.com/terms-and-conditions) on Wiley Online Library for rules of use; OA articles are governed by the applicable Creative Commons License

Therefore, when the length scale parameter h is chosen to be equal to γ, it is ensured that the macroscopic jump is equal to the microscopic jump ($[\![\boldsymbol{u}^M]\!] = [\![\hat{\boldsymbol{u}}]\!]$) in the fully failed state, independent of the RVE size.

4.1.2 | Extra remark on the macroscopic representation of the microscopic crack

When the micromodel is embedded in a full multiscale framework (as described in Section 2) and strain localization occurs, a discrete crack is inserted at the macroscale. Since at the macroscale a single (and thus constant) jump $[\![\boldsymbol{u}^M]\!]$ and normal $\boldsymbol{n}_\Gamma^M$ is related to a macroscopic material *point* that represents the microscopic domain Ω, it is implicitly assumed that the microscopic crack inside the RVE can be considered as a straight crack on the macroscale in an averaged sense. From the derivation presented above, it is shown that the microscopic (tortuous) crack can indeed be represented by a straight macroscopic crack with length 2R that crosses opposing points on the edge and consequently runs through the middle of the RVE (see Figure 4).

Throughout the rest of this article, the newly proposed PBCs (Equation 8) are denoted as *modified periodic boundary conditions* (*mod*-PBCs).

5 | NUMERICAL SIMULATIONS

In this section, the new formulation of periodicity on a circular micromodel is tested with numerical simulations. First, a description is provided of the heterogeneous RVEs, the material properties and the microscale constitutive models. In the first numerical example, the new formulation of PBCs is compared with the existing formulation by Glüge et al.[12] In the second numerical example, the new formulation is studied with a statistical analysis where six RVE sizes and 30 realizations per size are considered. For comparison purposes, the well-established square RVE with classical PBCs and periodic microstructure is used as a reference. Next, the ability of the new formulation to provide a transversely isotropic response is studied. Finally, the *unknown* jump in Equation (8) is studied in further detail in the last numerical example.

5.1 | Model preliminaries

5.1.1 | Heterogeneous circular and square RVEs

The heterogeneous micromodels that are considered consist of two material phases: matrix and randomly distributed circular fibers or inclusions. As part of this work, a definition is presented for a circular heterogeneous RVE that is similar to a periodic microstructure (see Figure 5), by allowing inclusions to cross the edge and letting exiting inclusions re-enter on the opposite side, such that a mixed-coupling of matrix-inclusion between opposing points is prevented and that each node has an associated node on the opposite side.

Since there is a slight overlap of inclusions that exit the edge and reappear on the other side, these inclusions on the boundary occupy slightly more area than the inclusions inside the domain that do not cross the edge. Consequently, different volume fractions can be obtained with the same number of inclusions in the RVE. This is not the case with the square RVE realizations, where the number of inclusions determines the volume fraction for a given RVE size. In order to keep the volume fraction constant for all realizations, the height of the square RVEs is determined from an integer number of inclusions and the volume fraction. Subsequently, circular RVE sizes with approximately the same areas as the square RVEs are determined. The inclusions have a diameter of 0.1 mm and the volume fraction is chosen as $\rho = 50\%$. This choice for the volume fraction is close to the maximum ratio that can be reached with the simple algorithm that is used in this study to obtain the circular RVEs. In order to keep the quality of the mesh, a maximum distance of 0.005 mm between inclusion edges is prescribed.

The geometric properties of six RVE sizes shown in Figure 6 are summarized in Table 1.[†] The material properties are tabulated in Table 2.[‡] In all cases, the same discretization is used. The domain is discretized with constant strain triangular elements with single point Gauss integration rules and a typical size of 0.02 mm.

10970207, 0, Downloaded from https://onlinelibrary.wiley.com/doi/10.1002/nme.7142 by Tu Delft, Wiley Online Library on [22/11/2022]. See the Terms and Conditions (https://onlinelibrary.wiley.com/terms-and-conditions) on Wiley Online Library for rules of use; OA articles are governed by the applicable Creative Commons License

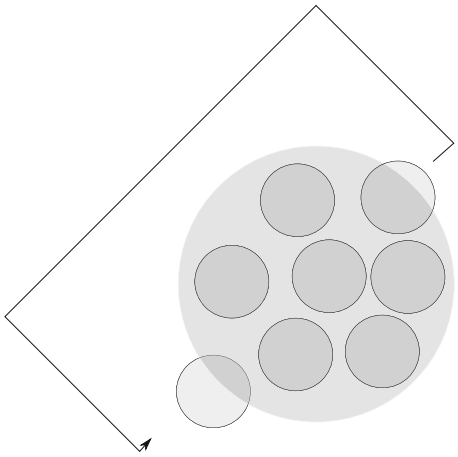

FIGURE 5 A circular RVE with periodic material. When an inclusion crosses the edge, a copy is mapped tot the opposite side.

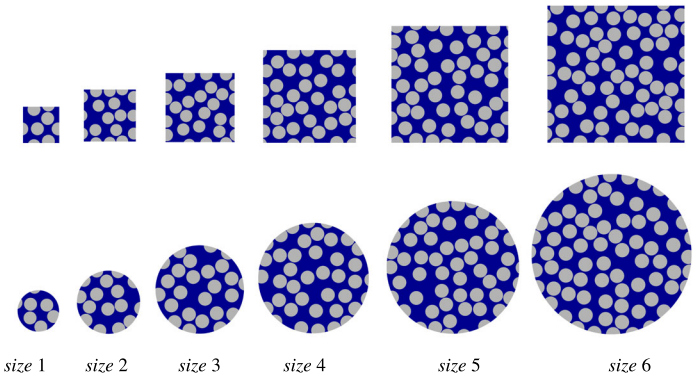

FIGURE 6 RVE sizes

TABLE 1 Geometric properties of the RVEs

	Square						Circular					
Size	**1**	**2**	**3**	**4**	**5**	**6**	**1**	**2**	**3**	**4**	**5**	**6**
Height (mm)	0.561	0.868	1.12	1.40	1.68	1.97	0.640	0.954	1.27	1.59	1.91	2.22
Area (mm^2)	0.314	0.754	1.26	1.95	2.83	3.90	0.322	0.715	1.27	1.99	2.87	3.87

5.1.2 | Microscale material model

The material model adopted for the inclusions is an isotropic linear elastic constitutive model while the matrix material is modeled with a mesh-size independent and fracture energy regularized isotropic CDM with linear softening (see Figure 7). Furthermore, the analyses are based on the small-strain assumption and a quasi-static loading. In the following, a brief description of the CDM is provided, according to Reference 20.

The (total) stress–strain relation can be expressed as

$$\boldsymbol{\sigma} = (1 - \omega)\boldsymbol{D}_e : \boldsymbol{\varepsilon}, \tag{18}$$

where $\boldsymbol{D}_e$ is the elastic stiffness matrix and ω is the damage parameter. The damage parameter is related to the history parameter κ, which keeps track of the highest equivalent strain $\tilde{\varepsilon}$ ever experienced by the material. A linear damage

10970207, 0, Downloaded from https://onlinelibrary.wiley.com/doi/10.1002/nme.7142 by Tu Delft, Wiley Online Library on [22/11/2022]. See the Terms and Conditions (https://onlinelibrary.wiley.com/terms-and-conditions) on Wiley Online Library for rules of use; OA articles are governed by the applicable Creative Commons License

TABLE 2 Material properties

Phase	Youngs' modulus E	Poisson's ratio ν	Tensile strength f_t	Fracture energy G_c
Inclusion	12,970 MPa	0.46	–	–
Matrix	4000 MPa	0.15	50 MPa	10 kJ/m^2

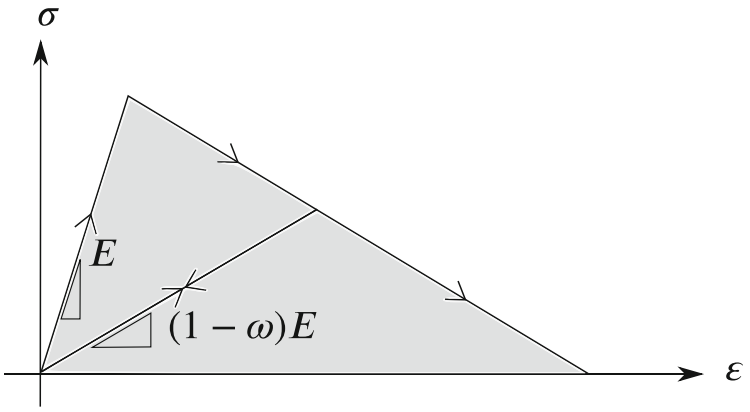

FIGURE 7 Bilinear damage model in 1D

evolution law is used and can be described as

$$\omega(\kappa) = \begin{cases} 0, & \text{if } \kappa < \kappa_i, \\ \frac{\kappa_u}{\kappa}\frac{\kappa-\kappa_i}{\kappa_u-\kappa_i}, & \text{if } \kappa_i \le \kappa < \kappa_u, \\ 1, & \text{if } \kappa \ge \kappa_u, \end{cases} \tag{19}$$

where $\omega = 0$ corresponds to no damage before the damage threshold κ_i and $\omega = 1$ corresponds to complete material failure at the ultimate value of κ_u. The damage threshold is defined as $\kappa_i = \frac{f_t}{E}$ and the ultimate strain as $\kappa_u = \frac{2G_c}{f_t l_e}$, where f_t, E, and G_c are the fracture strength, Young's modulus, and the fracture energy of the material, respectively, and l_e is a measure for the size of the element to obtain solutions that are mesh-size independent. For studying mode-I localization as a result of uniaxial strain, the *Mazars* equivalent strain measure is used to trigger crack opening, which is defined as

$$\tilde{\varepsilon} = \sqrt{\sum_{i=1}^{3}(\langle\varepsilon_i\rangle)^2}, \tag{20}$$

where ε_i is the principal strains with $\langle\varepsilon_i\rangle = \varepsilon_i$ in the case of tension ($\varepsilon_i > 0$) and $\langle\varepsilon_i\rangle = 0$ in the case of compression ($\varepsilon_i < 0$). For studying mode-II localization, the *von Mises* equivalent strain measure is used to obtain shear bands, defined as

$$\tilde{\varepsilon} = \frac{1}{2}\sqrt{\frac{12}{(1+\nu)^2}J_2^{\varepsilon}}, \tag{21}$$

where J_2^{ε} is the second invariant of the deviatoric strain tensor.

5.1.3 | Load cases

Two different load cases are defined, where the strain paths and material models are chosen such that the first case describes mode-I (opening) failure and the second case describes mode-II (sliding) failure (see Figure 8), denoted as *load*

10970207, 0, Downloaded from https://onlinelibrary.wiley.com/doi/10.1002/nme.7142 by Tu Delft, Wiley Online Library on [22/11/2022]. See the Terms and Conditions (https://onlinelibrary.wiley.com/terms-and-conditions) on Wiley Online Library for rules of use; OA articles are governed by the applicable Creative Commons License

case A and *load case B*, respectively. The load cases and the constitutive laws are summarized in Table 3. The components of the *equivalent* macroscopic strain $\boldsymbol{\mathcal{E}}^M$ are in terms of a local coordinate system, which is rotated with an angle θ with respect to the global coordinate system (see Figure 9).

Since the modes of deformation are a priori known, the macroscopic crack normal vector $\boldsymbol{n}_\Gamma^M$ can be provided in order to predefine the node pair $\{\hat{\boldsymbol{x}}^+, \hat{\boldsymbol{x}}^-\}$ on the circular RVE (see Figure 4). In load case A, the normal always points in the direction of $\bar{x}$ (see Figure 9). In load case B, there are two possible orientations for the shear band, with normal along $\bar{x}$ or along $\bar{y}$. In the current implementation of the *mod*-PBCs, without adaptive detection of the localization orientation, the node pair $\{\hat{\boldsymbol{x}}^+, \hat{\boldsymbol{x}}^-\}$ is selected to support a shear band with normal vector $\boldsymbol{n}_\Gamma^M$ in $\bar{x}$-direction.

5.2 | Example A: Comparison of the existing formulation by Glüge et al. and the new formulation of PBCs on a circular RVE

5.2.1 | Study description

In this example, the existing formulation proposed by Glüge et al.[12] is compared with the new formulation presented in Section 4. A circular RVE of *size* 5 is used (see Figure 6) and subjected to a uniaxial macroscopic strain under orientation angle $\theta = 0°$ (load case A in Table 3).

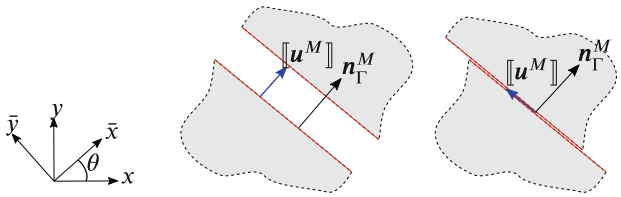

FIGURE 8 Macroscopic kinematics after localization that are transferred to the micromodel. Left: Mode-I localization. Right: Mode-II localization. When the macroscopic bulk strain is zero, the *equivalent* macroscopic strain is $\boldsymbol{\mathcal{E}}^M = \frac{1}{h}[\![\boldsymbol{u}^M]\!] \otimes^s \boldsymbol{n}_\Gamma^M$. Note that in the case of mode-I localization $\mathcal{E}_{\bar{x}\bar{y}}^M = \mathcal{E}_{\bar{y}\bar{x}}^M = 0$, $\mathcal{E}_{\bar{x}\bar{x}}^M \neq 0$, $\mathcal{E}_{\bar{y}\bar{y}}^M = 0$ and in the case of mode-II localization $\mathcal{E}_{\bar{x}\bar{y}}^M = \mathcal{E}_{\bar{y}\bar{x}}^M \neq 0$, $\mathcal{E}_{\bar{x}\bar{x}}^M = 0$, $\mathcal{E}_{\bar{y}\bar{y}}^M = 0$

TABLE 3 Load cases and constitutive models

Load case	Deformation	Imposed macro strain $\boldsymbol{\mathcal{E}}^M$	Equivalent strain $\tilde{\varepsilon}$	Localization mode
A	Uniaxial tension	$\begin{bmatrix} \mathcal{E}_{\bar{x}\bar{x}}^M & 0 \\ 0 & 0 \end{bmatrix}$	*Mazars*	Mode-I (opening)
B	Pure shear	$\begin{bmatrix} 0 & \mathcal{E}_{\bar{x}\bar{y}}^M \\ \mathcal{E}_{\bar{x}\bar{y}}^M & 0 \end{bmatrix}$	*von Mises*	Mode-II (sliding)

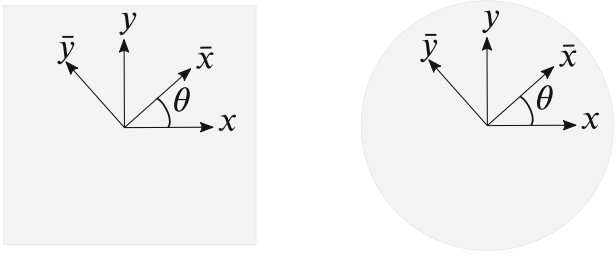

FIGURE 9 Local $\bar{x}, \bar{y}$-coordinate system rotated with angle θ with respect to the global x, y-coordinate system of the square and circular RVE

10970207, 0, Downloaded from https://onlinelibrary.wiley.com/doi/10.1002/nme.7142 by Tu Delft, Wiley Online Library on [22/11/2022]. See the Terms and Conditions (https://onlinelibrary.wiley.com/terms-and-conditions) on Wiley Online Library for rules of use; OA articles are governed by the applicable Creative Commons License

5.2.2 | Results and discussions

The resulting stress–strain responses and the post-peak deformation modes for both formulations are presented in Figure 10. It can be observed that the application of the existing constraint equations (Equation (2)) on a circular RVE results in a spurious hardening response instead of the physically realistic softening response. A single dominant localization band is not supported since cracks cannot cross the boundary, which results in severe over-constraining after the onset of damage and prevents global softening with a homogenized stress that goes to zero. This numerical result demonstrates the consequences of the analysis in Section 3, where it is shown that the existing constraint equations do not support the desired final mode of a separation in two unloaded hemicircles. It can be observed the new formulation of PBCs on a circular RVE allows for a fully developed crack to cross the boundary and therefore successfully removes this over-constraining effect.

5.3 | Example B: RVE size statistical study

5.3.1 | Study description

In this numerical example, square and circular RVEs with six sizes (see Figure 6) are subjected to a uniaxial macroscopic strain under orientation angle $\theta = 0°$ (load case A in Table 3). For every size, 30 different realizations of random fiber distribution are considered.

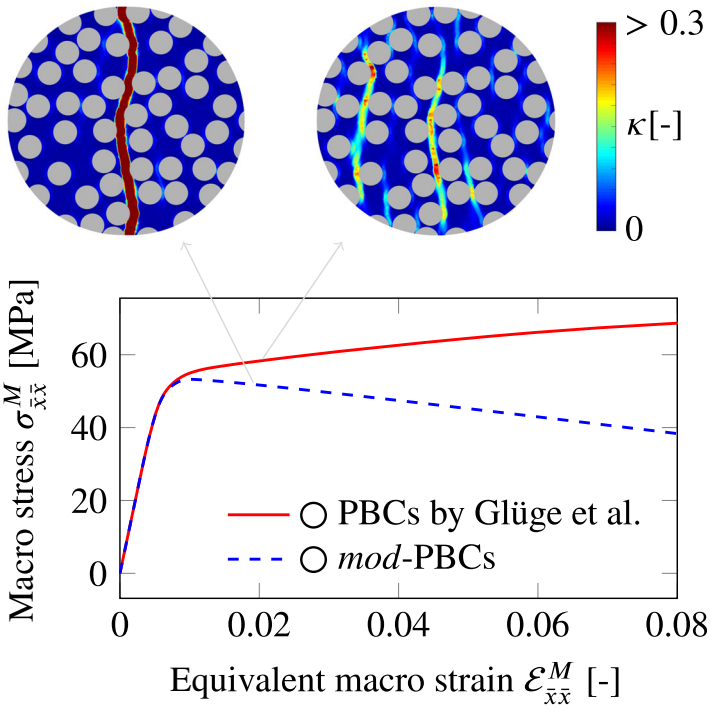

FIGURE 10 Stress–strain response obtained with the existing formulation proposed by Glüge et al.[12] and the new formulation (*mod*-PBCs) proposed in this work. The corresponding contour plot of the history variable κ is provided at an *equivalent* macroscopic strain of $\mathcal{E}^M_{\bar{x}\bar{x}} = 0.02$.

10970207, 0, Downloaded from https://onlinelibrary.wiley.com/doi/10.1002/nme.7142 by Tu Delft, Wiley Online Library on [22/11/2022]. See the Terms and Conditions (https://onlinelibrary.wiley.com/terms-and-conditions) on Wiley Online Library for rules of use; OA articles are governed by the applicable Creative Commons License

5.3.2 | Results and discussions

The stress–strain curves from all realizations of the smallest (*size* 1) and the largest (*size* 6) RVEs are presented in Figure 11. It can be observed that for both RVE shapes the scatter in the response is much lower with the largest compared to the smallest size of the RVEs, which is expected since statistical representativeness increases with larger RVEs.

The sample mean and standard deviations of the peak stress and the corresponding strain value are depicted in Figure 12. It can again be observed that the scatter in peak stresses and corresponding strain values reduce as the RVE sizes increase for both the square and the circular RVE.

Another observation from Figure 12 is that with the circular RVEs, the peak tends to occur at a lower strain compared to the square RVEs. As a direct consequence of the formulation, micro cracks are only allowed to cross the edges at two unique opposing points. This can also be observed from Figure 13, where the damage variable ω is plotted for a typical square and circular RVE of *size* 6. The square RVE does allow for multiple micro cracks along the boundary, as long as they are periodic, whereas the circular RVE only allows cracks to cross the edge in elements where the final crack band is allowed. Therefore, even with the improved formulation where a complete softening response is permitted, pre-peak hardening is stiffer for the circular RVE than for the square RVE. This stiffer pre-peak hardening response can also be observed from Figure 14, which shows a typical stress–strain response of the square and circular RVE. In addition, this restriction of the crack to cross the boundary at only two opposing points, results in less competition between alternative crack paths in becoming the final crack that separates the circular RVE in two halves. This leads to less energy dissipation before the peak and consequently to a smaller hardening branch with earlier overall softening in the case of the circular RVE.

It can also be observed in Figure 12 that the circular RVEs tend to predict (slightly) higher peak stresses compared to the square RVEs. The crack band patterns after the peak stress of five RVEs with *size* 5 are shown in Figure 15. This figure shows that the crack bands inside the circular RVEs are more tortuous. For some cases, a (slight) mixed-mode deformation instead of a pure mode-I deformation, is obtained as a result of the formulation where $\overline{\boldsymbol{n}}_\Gamma$ is adjusted when an inclusion exists on the RVE edge (as described in Section 4), which results in more scatter in the peak stress compared to the square RVEs (see Figure 12). However, this effect of slight mixed-mode localization reduces as the RVE

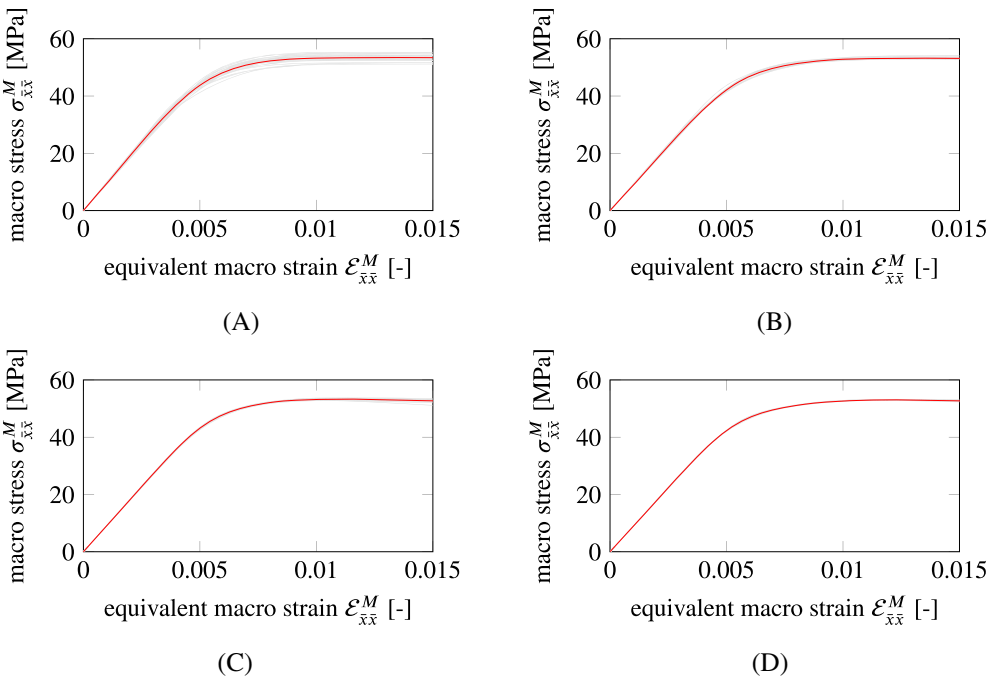

FIGURE 11 Stress–strain curves from all RVE realizations of the smallest (*size* 1) and largest RVEs (*size* 6). The mean of the RVE responses is shown in red and the response of each realization is shown in light gray. (A) Circular RVE *size* 1, (B) square RVE *size* 1, (C) circular RVE *size* 6, and (D) square RVE *size* 6

10970207, 0, Downloaded from https://onlinelibrary.wiley.com/doi/10.1002/nme.7142 by Tu Delft, Wiley Online Library on [22/11/2022]. See the Terms and Conditions (https://onlinelibrary.wiley.com/terms-and-conditions) on Wiley Online Library for rules of use; OA articles are governed by the applicable Creative Commons License

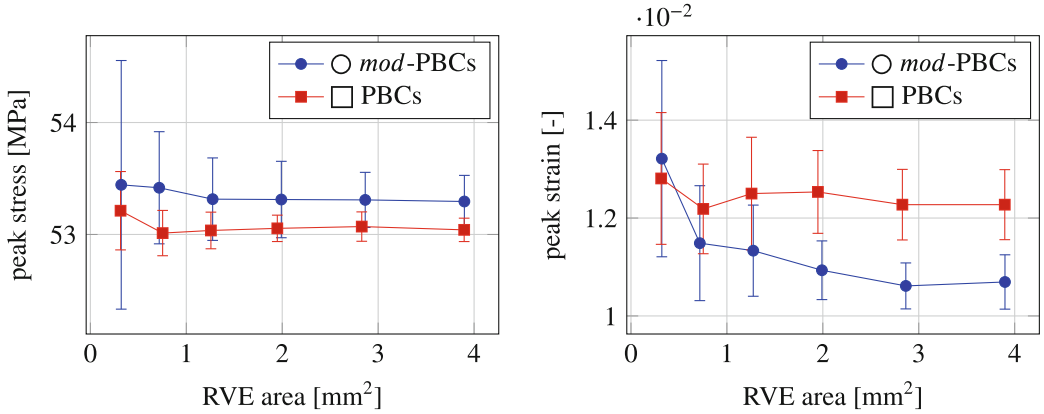

FIGURE 12 Results of the statistical analysis. The sample mean plus and minus the sample standard deviation is shown for each RVE size and shape. The sample mean and standard deviations of variable x are computed as $\mu_x = \frac{1}{N}\sum_{i=1}^{N} x_i$ and $\sigma_x = \sqrt{\frac{1}{N-1}\sum_{i=1}^{N}(x_i - \mu_x)^2}$, respectively.

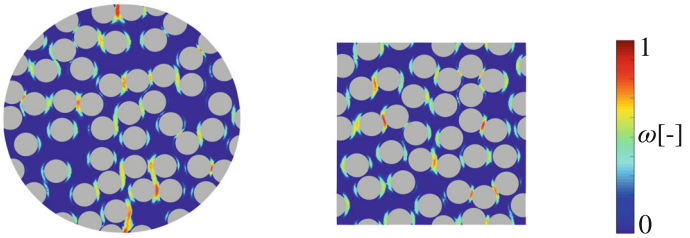

FIGURE 13 Damage plots at the moment of the peak of the circular RVE at *equivalent* macroscopic strain $\mathcal{E}^M_{\bar{x}\bar{x}} = 0.008$

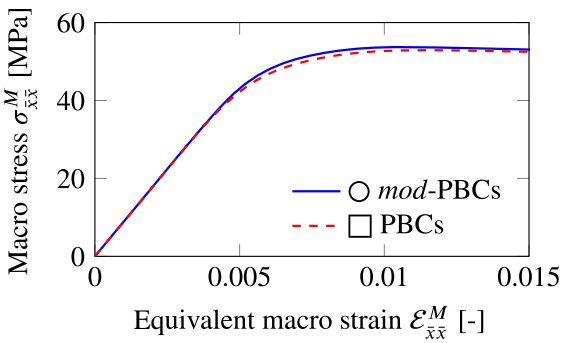

FIGURE 14 Typical stress–strain curve with two RVE realizations of *size* 6

size increases. As already addressed in the previous paragraph, the circular RVE severely restricts the number of possible crack bands, since cracks are only allowed to cross the edges at two unique opposing locations. This is different from the square RVE where a crack band with a certain orientation angle can cross opposing edges at multiple locations (see Figure 15). This kinematic restriction of the circular RVE over-constrains the response and may result in a final failure mechanism that is less critical, which contributes to the slightly higher mean values in peak stresses with the circular RVEs.

It is expected that upon further increasing the RVE size, the difference between the circular and the square RVE vanishes. However, since the statistical representativeness of the circular RVE is determined by the number of inclusions in the (small) region where a crack band is allowed to develop and cross the edge, and not in the overall volume as with square RVEs, it is expected that convergence is much slower with circular RVEs.

10970207, 0, Downloaded from https://onlinelibrary.wiley.com/doi/10.1002/nme.7142 by Tu Delft, Wiley Online Library on [22/11/2022]. See the Terms and Conditions (https://onlinelibrary.wiley.com/terms-and-conditions) on Wiley Online Library for rules of use; OA articles are governed by the applicable Creative Commons License

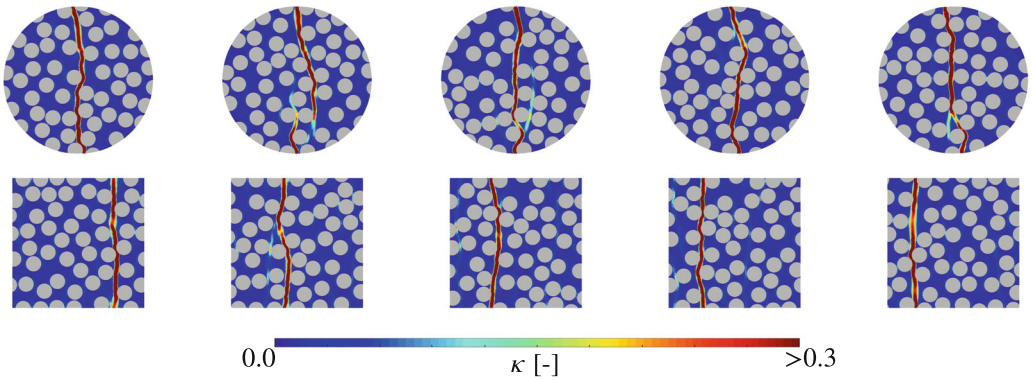

FIGURE 15 Contours of history variable κ with five realizations of RVE *size* 5 at *equivalent* macroscopic strain $\mathcal{E}^M_{\overline{xx}} = 0.020$

5.4 | Example C: Isotropy study

5.4.1 | Study description

In this example, a uniaxial strain and a shear strain (load case A and B in Table 3) are applied on the RVEs under 20 different angles $\theta(^\circ) \in \{0, 5, \ldots, 90\}$. For this purpose, a circular RVE of *size* 5 is used (see Figure 6). For each orientation angle θ, the *equivalent* macroscopic strain is rotated to the global x, y-coordinate system and applied on the RVEs. After solving the microscopic BVPs, the global stress–strain components are transformed to the local $\overline{x}, \overline{y}$-coordinate system and used for comparing the response of the square and the circular RVEs.

In the previous example, RVEs with equal volumes (area with unit thickness) were studied, in order to establish a fair comparison in the pre-peak regime. However, in this study the RVEs are loaded until complete failure of the material is reached. The well-known deterministic size effect in the homogenized stress–strain response in the case of localization[14] is taken into account for comparing the stress–strain curves obtained with the circular and square RVEs and corresponding BCs. This is done by generating another square RVE with a height of 1.5 mm for this example, such that the ratio of the height over the volume is equal for both RVE shapes and the amount of energy dissipation in the case of a vertical crack in the circular and square RVE is similar.

5.4.2 | Results and discussions

The development of the crack bands for both the square and the circular RVE, as a result of the load cases A and B under orientation angle $\theta = 25^\circ$, is shown in Figures 16 and 17, respectively. It can be observed from these figures that the circular RVE supports a single inclined crack band, whereas multiple inclined bands appear in the square RVE. Moreover, Figure 17 shows that the sliding of the circular and square RVE in Figure 17 is in different directions. In the current implementation of the *mod*-PBCs, the normal $\boldsymbol{n}^M_\Gamma$ is not detected on the fly but a priori prescribed. Therefore, the sliding direction is always in the direction along $\overline{x}$ (as described in Section 5.1.3), which is not the case with the square RVE where two orthogonal shear band orientations are possible solutions.

The localization patterns for several loading orientation angles θ, are depicted in Figures 18 and 19. It can be observed from these figures that the circular RVE supports the development of a single inclined localization band for all orientation angles, while in the square RVE, multiple (periodic) localization bands occur if the orientation angle is not $\theta = 0^\circ, 45^\circ$, or 90°.

The stress–strain curves (in local coordinates) as a result of load cases A and B with all loading orientation angles θ are presented in Figures 20 and 21. For each loading orientation angle θ, the stress values at the peak and after the peak (at an applied *equivalent* macroscopic strain $\mathcal{E}^M_{\overline{xx}} = 0.15$) are given in the stress versus load orientation curves. It can be observed that with both load cases, the variation in post-peak stresses is far less with the circular RVE than with the square RVE. This confirms that the qualitative difference in crack pattern for different load directions significantly affects the homogenized response of the square RVE, while the circular RVE with

10970207, 0, Downloaded from https://onlinelibrary.wiley.com/doi/10.1002/nme.7142 by Tu Delft, Wiley Online Library on [22/11/2022]. See the Terms and Conditions (https://onlinelibrary.wiley.com/terms-and-conditions) on Wiley Online Library for rules of use; OA articles are governed by the applicable Creative Commons License

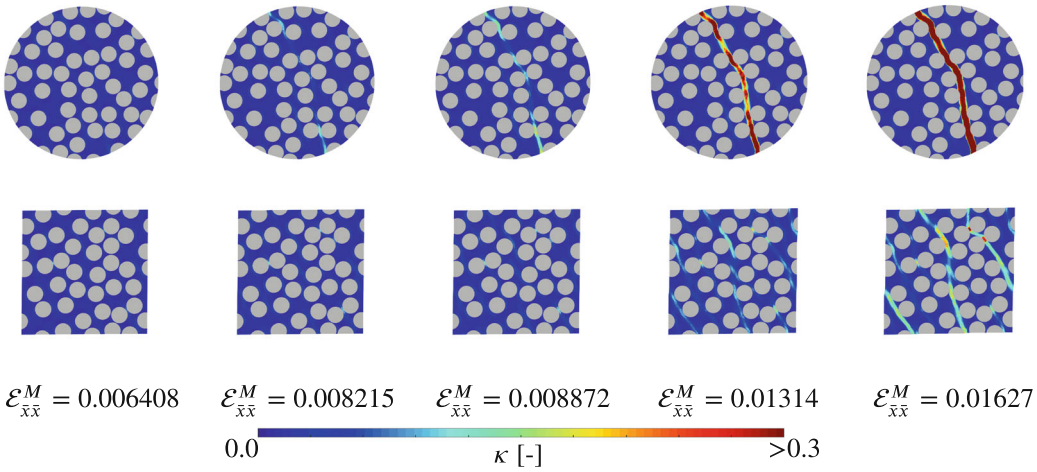

FIGURE 16 Development of localization (mode-I) as a result of load case A and orientation angle $\theta = 25°$ with contour plots of history variable κ

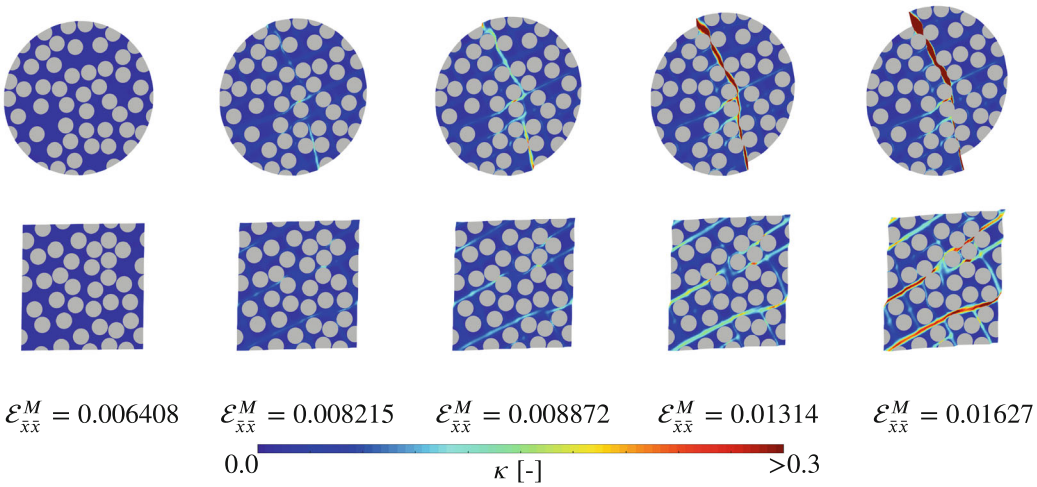

FIGURE 17 Development of localization (mode-II) as a result of load case B and orientation angle $\theta = 25°$ with contour plots of history variable κ

qualitatively similar crack pattern for all load directions indeed translates to a direction-independent stress–strain relation.

The orientation-dependence of the averaged stress–strain response during softening is at least partially due to the change in crack length. It is known that consistent upscaling of the softening response requires usage of a scaling factor h (see Equation (1)), which should be defined as the area of the RVE divided by the effective length of the projected crack band through the RVE.[6,7,11] In order to study to which extent the observed orientation-dependence can be attributed to the lack of such scaling in the presented stress–strain plots, an additional postprocessing step is performed to generate stress-opening plots. Using the homogenized stiffness E from the initial phase of the RVE simulation, ε^M_b can be estimated from σ^M/E after which $[\![u^M]\!]$ can be obtained with Equation (1) when h is known (see Figure 22). For h we use the definition proposed by Svenning et al.,[7] which assumes the presence of a single localization band that crosses the RVE:

$$h \equiv \begin{cases} \sqrt{|\Omega|}\ \cos\ \theta, & 0° \leq \theta \leq 45°, \\ \sqrt{|\Omega|}\ \sin\ \theta, & 45° \leq \theta \leq 90°. \end{cases} \tag{22}$$

10970207, 0, Downloaded from https://onlinelibrary.wiley.com/doi/10.1002/nme.7142 by Tu Delft, Wiley Online Library on [22/11/2022]. See the Terms and Conditions (https://onlinelibrary.wiley.com/terms-and-conditions) on Wiley Online Library for rules of use; OA articles are governed by the applicable Creative Commons License

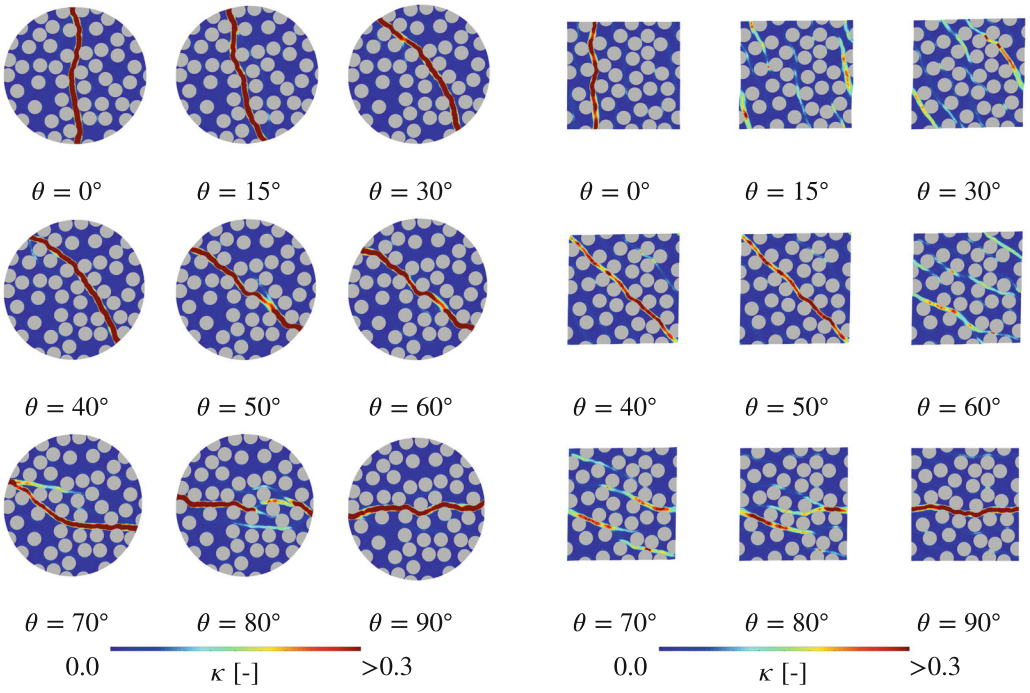

FIGURE 18 RVE crack band patterns corresponding to load case A at $\mathcal{E}^M_{\overline{xx}} = 0.02$

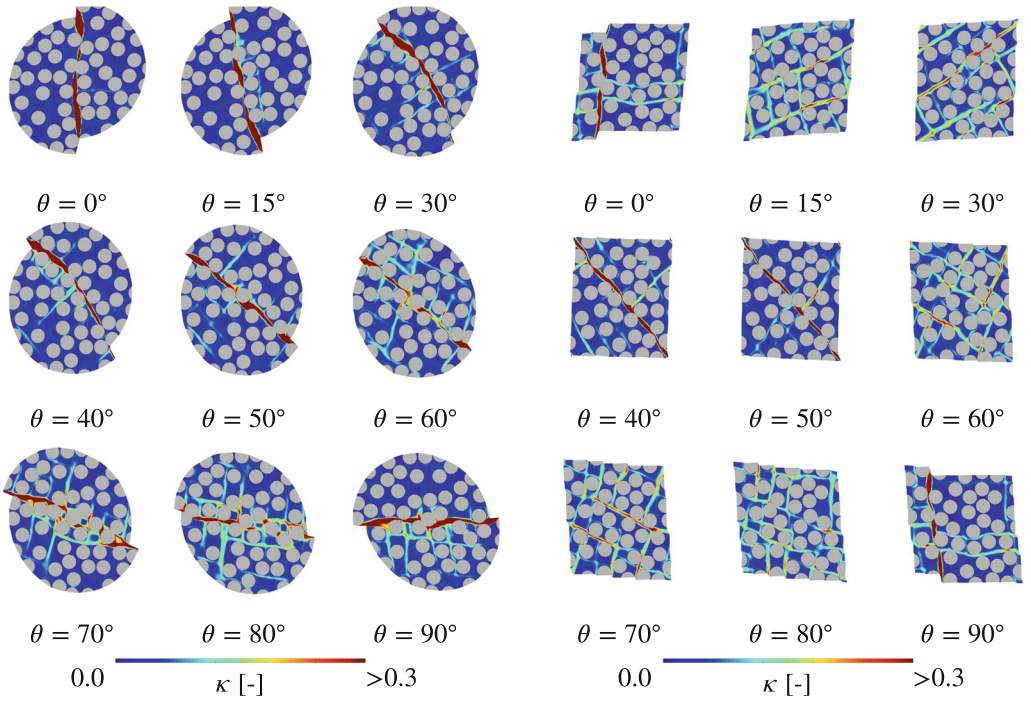

FIGURE 19 RVE crack band patterns corresponding to load case B at $\mathcal{E}^M_{\overline{xy}} = 0.04$

10970207, 0, Downloaded from https://onlinelibrary.wiley.com/doi/10.1002/nme.7142 by Tu Delft, Wiley Online Library on [22/11/2022]. See the Terms and Conditions (https://onlinelibrary.wiley.com/terms-and-conditions) on Wiley Online Library for rules of use; OA articles are governed by the applicable Creative Commons License

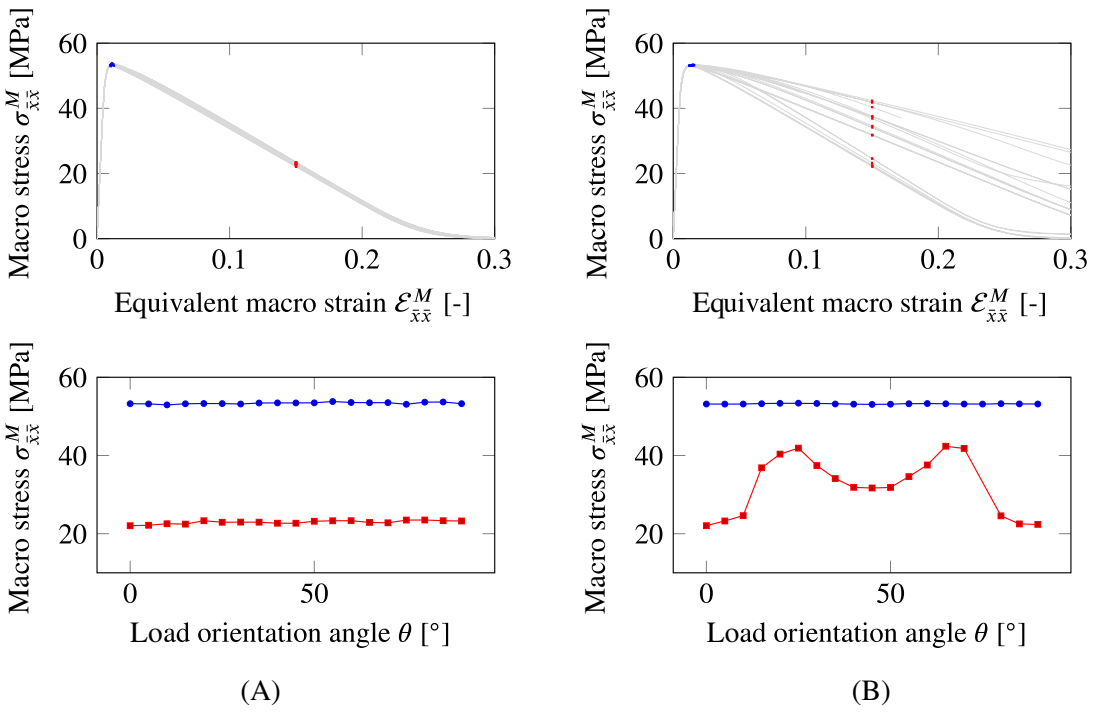

FIGURE 20 Stress–strain (top) and stress–orientation curves (bottom) corresponding to load case A. (A) Circular RVE with mod-PBCs and (B) square RVE with PBCs

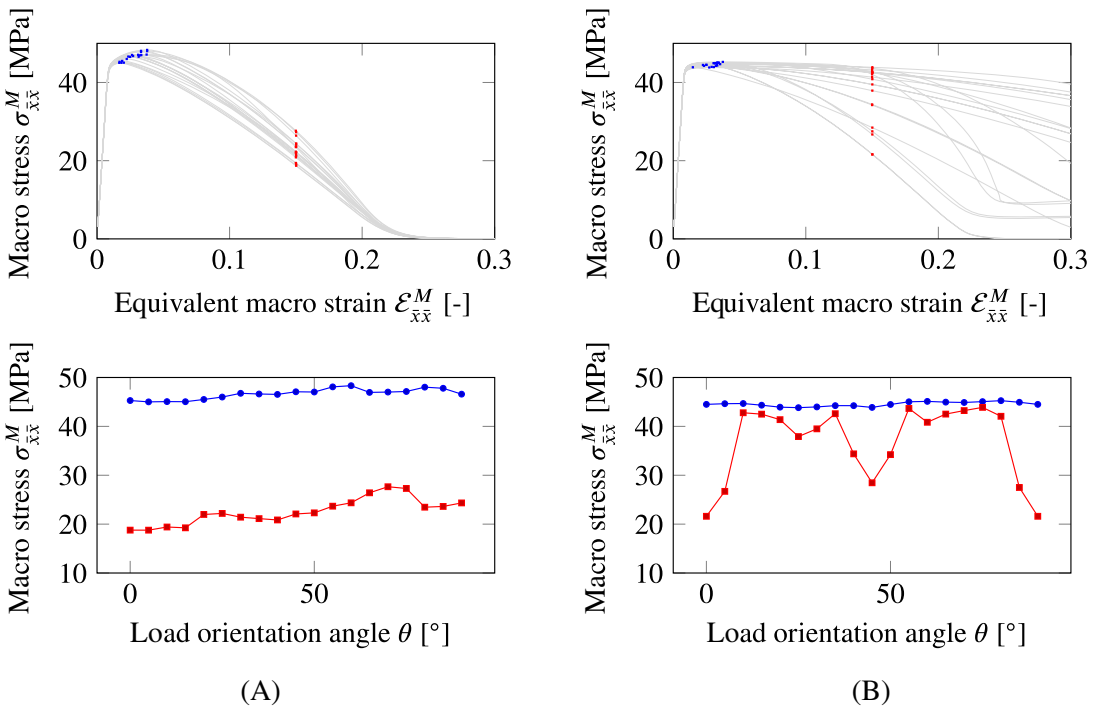

FIGURE 21 Stress–strain (top) and stress–orientation curves (bottom) corresponding to load case B. (A) Circular RVE with mod-PBCs and (B) square RVE with PBCs

10970207, 0, Downloaded from https://onlinelibrary.wiley.com/doi/10.1002/nme.7142 by Tu Delft, Wiley Online Library on [22/11/2022]. See the Terms and Conditions (https://onlinelibrary.wiley.com/terms-and-conditions) on Wiley Online Library for rules of use; OA articles are governed by the applicable Creative Commons License

The resulting stress-opening and stress–orientation curves (with stress values corresponding to $[\![u^M]\!] = 0.10$) are shown in Figure 23. It can be observed that the orientation dependence is repaired for a loading angle θ of 45°, which gives in stress-opening space the same softening response as the 0° and 90° cases. For angles other than those, the orientation dependence remains, which is due to the fact that for these angles the assumption of a single localization band crossing the RVE is not valid. As argued in Section 1 and evidenced in Reference 5, methods that have been proposed to recover a single localization band under arbitrary angles by rotating or shifting the PBCs, do not always give orientation independent results either.

For shear loading (load case B), a larger scatter in strength with the circular RVE can be observed (see Figure 21). In the case of pure shear, multiple (orthogonal) potential shear bands satisfy the same imposed shear deformation via the BCs and the most critical one, depending on the individual realization of inclusions, becomes the actual final failure mode. However, in the current implementation of the *mod*-PBCs on a circular RVE, the node pair $\{\hat{\boldsymbol{x}}^+, \hat{\boldsymbol{x}}^-\}$ is selected a priori and is not determined on the fly, which limits the possibilities for a final failure mode and therefore negatively influences the statistical representativeness of the micromodel. In addition, by a priori selecting the node pair $\{\hat{\boldsymbol{x}}^+, \hat{\boldsymbol{x}}^-\}$ on the RVE, cracks are forced to propagate to these nodes which often results in relatively tortuous crack patterns. In the case of mode-II (sliding) failure, this tortuosity results in an obstruction of the sliding deformation. When the crack crosses a large amount of (stiff) inclusions (compare orientation angle $\theta = 70°$ with $\theta = 0°$ in Figure 19), the resistance against the sliding deformation is higher which results in a larger macroscopic stress.

Since this variation in strength with the circular RVE is related to a single realization, another set of 15 circular RVEs is generated. The post-peak stress of all realizations and the mean value of the stress at $\mathcal{E}_{\overline{xx}} = 0.15$ are presented in Figure 24. Since the mean value is almost a straight line, it is confirmed that the response of the circular RVE is independent on the orientation angle θ.

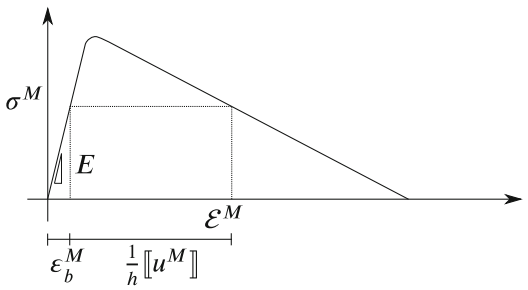

FIGURE 22 Back-computing the jump

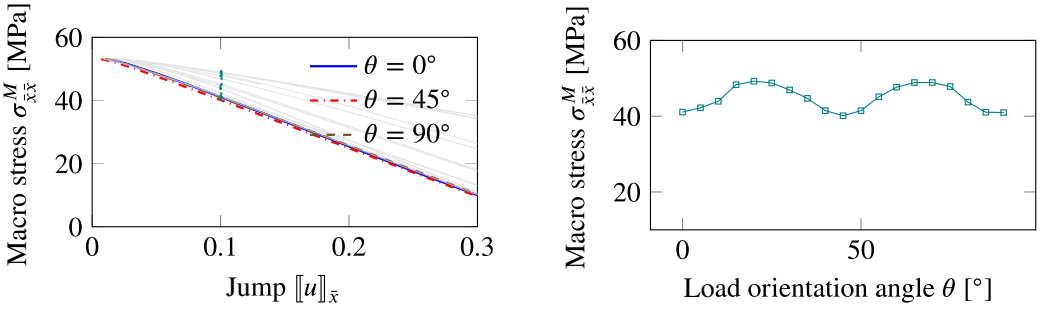

FIGURE 23 Stress–jump response of the square RVE and PBCs corresponding to load case A

10970207, 0, Downloaded from https://onlinelibrary.wiley.com/doi/10.1002/nme.7142 by Tu Delft, Wiley Online Library on [22/11/2022]. See the Terms and Conditions (https://onlinelibrary.wiley.com/terms-and-conditions) on Wiley Online Library for rules of use; OA articles are governed by the applicable Creative Commons License

5.5 | Example D: Jump study

5.5.1 | Study description

In this example, the *unknown* microscopic jump, that is present in the new formulation of PBCs on a circular RVE (see Equation 8), is studied in further detail. For this purpose, the same circular RVE as in the previous example is used and subjected to a uniaxial macroscopic strain under orientation angle $\theta = 0°$ (load case A in Table 3). The x-component of the micro jump $[\![\hat{u}]\!]_{\bar{x}}$ is monitored. In addition, the horizontal displacement of the rightmost node on the boundary, opposite to the fixed node on the left side, denoted as u^{end}, is tracked.

5.5.2 | Results and discussions

Both displacements $[\![\hat{u}]\!]_{\bar{x}}$ and u^{end} as functions of the applied *equivalent* macroscopic strain $\mathcal{E}^M_{\bar{x}\bar{x}}$ are shown in Figure 25. From these figures, it can be observed that $u^{\text{end}}_{\bar{x}}$ initially follows the line $2R\mathcal{E}^M_{\bar{x}\bar{x}}$, while $[\![\hat{u}]\!]_{\bar{x}}$ remains approximately zero. However, as soon as localization occurs, $[\![\hat{u}]\!]_{\bar{x}}$ becomes gradually nonzero and $u^{\text{end}}_{\bar{x}}$ starts to trace the line of $\gamma\mathcal{E}^M_{\bar{x}\bar{x}}$, and eventually coincides with it. This is a direct consequence of the extra kinematic freedom that is provided by the new formulation Equation (8), which allows for a realistic final failure mode when $\boldsymbol{\mathcal{E}}^M - \hat{\boldsymbol{\varepsilon}} = 0 \rightarrow \frac{1}{\gamma}[\![\hat{\boldsymbol{u}}]\!] \otimes^s \boldsymbol{n}^M_\Gamma = \boldsymbol{\mathcal{E}}^M$.

3D plots of the displacement in x-direction at two different time instances are shown in Figure 26. From the 3D plots, it can be observed that the kinematic restriction provided by the surrounding material is realistically taken into account with the new formulation on a circular domain, by allowing microfluctuations to exist on the RVE edge. In addition, cross-sections are provided where the x-components of the displacements of the nodes that are close to the line $y = 0$, are plotted. It can be observed that before localization, the deformation is described as the macroscopic strain plus a smooth

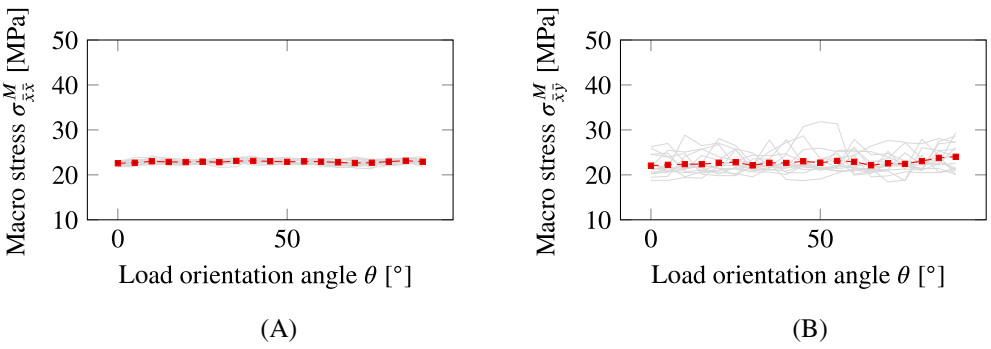

FIGURE 24 Stress–orientation curves of 15 samples of circular RVEs. The mean response is shown in red and the response of each realization is shown in light gray. (A) Load case A and (B) load case B

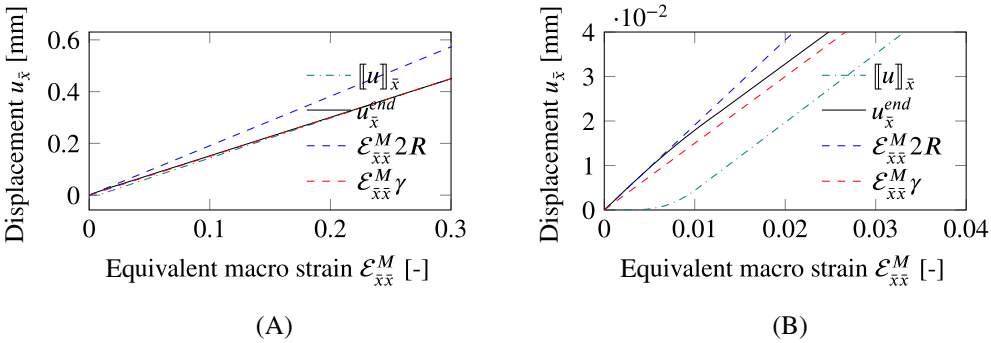

FIGURE 25 Microscopic jump and displacement of a node with the largest displacement in x as a function of the *equivalent* macroscopic strain $\mathcal{E}^M_{\bar{x}\bar{x}}$. The red and blue dashed lines are added to the figure as a reference. (A) Full curves and (B) zoomed portion

10970207, 0, Downloaded from https://onlinelibrary.wiley.com/doi/10.1002/nme.7142 by Tu Delft, Wiley Online Library on [22/11/2022]. See the Terms and Conditions (https://onlinelibrary.wiley.com/terms-and-conditions) on Wiley Online Library for rules of use; OA articles are governed by the applicable Creative Commons License

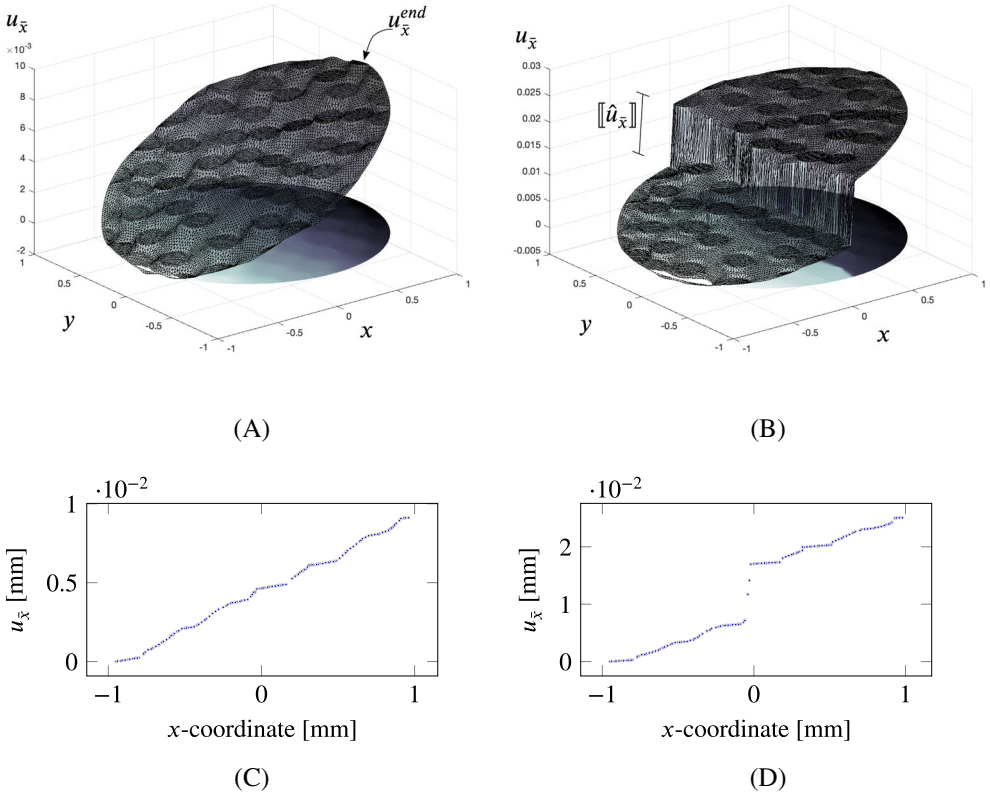

FIGURE 26 Three-dimensional plots and corresponding cross-sections along $y = 0$ of the displacements in x-direction. (A) 3D plot before localization, (B) 3D plot after localization, (C) cross-section before localization, and (D) cross-section after localization

microscopic fluctuation due to the heterogeneities. The deformations shown for after localization correspond to a time step after the peak but before complete softening, where the total deformation is composed of the bulk strain that is still perturbed by a smooth fluctuation and the displacement jump across the localization band.

6 | CONCLUSIONS

In this article, a new formulation for PBCs on a circular RVE is presented that restores transverse isotropy of the micromodel by allowing for fully localized deformations under an arbitrary angle.

The existing formulation of PBCs on a spherical RVE as proposed in literature, is tested in a two-dimensional setting on a circular RVE with analytical and numerical examples. It is shown that the formulation does not allow crack bands to cross the RVE boundary and consequently prevents a full softening response. It is demonstrated through numerical simulations that with the new formulation of PBCs on a circular RVE, the full softening response is recovered and that the response is fully transversely isotropic, unlike with commonly used square RVEs. Moreover, a new definition of a circular heterogeneous RVE with periodic material is presented, where inclusions are allowed to cross the edge.

With a statistical analysis, it is shown that the circular RVE provides almost the same response as the square RVE, when a horizontal uniaxial imposed strain leads to a (single) vertical crack band in both RVEs. However, a slightly stiffer pre-peak hardening response is observed with the circular RVE, since local micro-cracks near the boundary are still suppressed at locations other than where the new formulation allows a dominant final crack to cross the RVE boundary at opposing points. These kinematic restrictions due to the BCs on the circular RVE contribute to an observed slower convergence compared to the square RVE with classical PBCs in the case of vertical localization bands.

Furthermore, the proposed method does not require a rotation or shifting of the microstructure, as is the case with previously developed approaches with square RVEs. Therefore, artificial reinforcement caused by a mismatch of the microstructure across coupled boundaries is avoided. Instead, an unknown jump is added to the periodic constraint

10970207, 0, Downloaded from https://onlinelibrary.wiley.com/doi/10.1002/nme.7142 by Tu Delft, Wiley Online Library on [22/11/2022]. See the Terms and Conditions (https://onlinelibrary.wiley.com/terms-and-conditions) on Wiley Online Library for rules of use; OA articles are governed by the applicable Creative Commons License

equations, which does not affect the response before localization and therefore provides a smooth transition to a localized state. Although it is not utilized in the numerical examples where the localization angle is a priori prescribed, this feature enables the possibility for extending the framework where the correct localization angle is determined on the fly and used to adapt the BCs, without causing abrupt changes in the imposed deformations. When the micromodel is embedded in a multiscale framework for strain localization, a macro jump and corresponding normal vector is provided as soon as localization is detected, for example, by monitoring the eigenvalues of the acoustic tensor. It is envisioned that the macroscopic normal vector of the crack can be used to determine the orientation of the crack through the micromodel and hence the location where the crack crosses the RVE boundary.

ENDNOTES

*Even when ensuring point symmetry of the microstructure along the edge, the microstructure cannot be interpreted as representing an infinite periodic system, because it is not possible to glue the circular RVE to copies of itself. However, since this periodicity of the material is artificial in the case of random microstructures[12] and is the direct cause of the orientation dependence where cracks are forced to be periodic as well, we do not consider this feature to be a disadvantage of the circular RVE. In addition, the BCs allow for a microfluctuation to exist on the boundary of the RVE. Therefore, the response is in between the static and kinematic bounds, similar to the PBCs applied to a square micromodel. In order to stay consistent with the terminology that is used in the literature for these BCs also in the context of circular micromodels,[12] we keep referring to the constraint equations as PBCs.

†For certain combinations of circular RVE sizes and inclusion radii it required an extreme amount of iterations of generating RVEs to get the volume fractions within the specified tolerance. Therefore, slightly perturbed areas are chosen in order to generate RVEs within a reasonable amount of time. This explains the small difference in area between both shapes and decimal values in Table 1.

‡During the process of this research, spurious (bending) modes were observed with large sized RVEs containing mesh-irregularities in combination with brittle material behavior. It is thought that this is related to the CDM, where localization sometimes takes place in more than one element on the boundary, which is not consistent with the assumption of a discrete crack between two nodes on either side of where the crack is allowed to cross the boundary. The expectation is that with a discrete crack model, this issue will be not be encountered. Since this is unrelated to the BCs, the material properties are chosen such that all simulations in this study could be carried out without triggering these spurious modes. For a more detailed description of these observed spurious modes, see Hofman.[19]

ACKNOWLEDGMENT

Financial support from the Dutch Research Council NWO under Vidi grant 16464 is gratefully acknowledged.

DATA AVAILABILITY STATEMENT

Data presented in this article are available at the 4TU. ResearchData repository through https://doi.org/10.4121/21304308.v1.

ORCID

Pieter Hofman https://orcid.org/0000-0001-6154-2776
Frans P. van der Meer https://orcid.org/0000-0002-6691-1259

REFERENCES

1. Van der Meer FP. Micromechanical validation of a mesomodel for plasticity in composites. *European Journal of Mechanics - A/Solids*. 2016;60:58-69. doi:10.1016/j.euromechsol.2016.06.008
2. Svenning E, Fagerström M, Larsson F. Localization aligned weakly periodic boundary conditions. *Int J Numer Methods Eng*. 2017;111(5):493-500. doi:10.1002/nme.5483
3. Goldmann J, Brummund J, Ulbricht V. On boundary conditions for homogenization of volume elements undergoing localization. *Int J Numer Methods Eng*. 2017;113(1):1-21. doi:10.1002/nme.5597
4. Coenen EWC, Kouznetsova VG, Geers MGD. Novel boundary conditions for strain localization analyses in microstructural volume elements. *Int J Numer Methods Eng*. 2011;90(1):1-21. doi:10.1002/nme.3298
5. Giesen Loo E, Van der Meer FP. Stress-controlled weakly periodic boundary conditions: axial stress under varying orientations. *Int J Numer Methods Eng*. 2020;121(19):4458-4470. doi:10.1002/nme.6441
6. Oliver J, Caicedo M, Roubin E, Huespe AE, Hernández JA. Continuum approach to computational multiscale modeling of propagating fracture. *Comput Methods Appl Mech Eng*. 2015;294:384-427. doi:10.1016/j.cma.2015.05.012
7. Svenning E, Larsson F, Fagerström M. Two-scale modeling of fracturing solids using a smeared macro-to-micro discontinuity transition. *Comput Mech*. 2017;60(4):627-641. doi:10.1007/s00466-017-1426-z
8. Svenning E, Larsson F, Fagerström M. A two-scale modeling framework for strain localization in solids: XFEM procedures and computational aspects. *Comput Struct*. 2019;211:43-54. doi:10.1016/j.compstruc.2018.08.003
9. Coenen EWC, Kouznetsova VG, Geers MGD. Multi-scale continuous-discontinuous framework for computational-homogenization-localization. *J Mech Phys Solids*. 2012;60(8):1486-1507. doi:10.1016/j.jmps.2012.04.002

10970207, 0, Downloaded from https://onlinelibrary.wiley.com/doi/10.1002/nme.7142 by Tu Delft, Wiley Online Library on [22/11/2022]. See the Terms and Conditions (https://onlinelibrary.wiley.com/terms-and-conditions) on Wiley Online Library for rules of use; OA articles are governed by the applicable Creative Commons License

10. Coenen EWC, Kouznetsova VG, Bosco E, Geers MGD. A multi-scale approach to bridge microscale damage and macroscale failure: a nested computational homogenization-localization framework. *Int J Fract*. 2012;178(1-2):157-178. doi:10.1007/s10704-012-9765-4
11. Ke L, Van der Meer FP. A computational homogenization framework with enhanced localization criterion for macroscopic cohesive failure in heterogeneous materials. *J Theor Comput Appl Mech*. 2022;2:1-28. doi:10.46298/jtcam.7707
12. Glüge R, Weber M, Bertram A. Comparison of spherical and cubical statistical volume elements with respect to convergence, anisotropy, and localization behavior. *Comput Mater Sci*. 2012;63:91-104. doi:10.1016/j.commatsci.2012.05.063
13. Geers MGD, Kouznetsova VG, Brekelmans WAM. Multi-scale computational homogenization: trends and challenges. *J Comput Appl Math*. 2010;234(7):2175-2182. doi:10.1016/j.cam.2009.08.077
14. Gitman IM, Askes H, Sluys LJ. Representative volume: existence and size determination. *Eng Fract Mech*. 2007;74(16):2518-2534. doi:10.1016/j.engfracmech.2006.12.021
15. Verhoosel CV, Remmers JJC, Gutiérrez MA, de Borst R. Computational homogenization for adhesive and cohesive failure in quasi-brittle solids. *Int J Numer Methods Eng*. 2010;83(8-9):1155-1179. doi:10.1002/nme.2854
16. Nguyen VP, Lloberas-Valls O, Stroeven M, Sluys LJ. Homogenization-based multiscale crack modelling: from micro-diffusive damage to macro-cracks. *Comput Methods Appl Mech Eng*. 2011;200(9-12):1220-1236. doi:10.1016/j.cma.2010.10.013
17. Nguyen VP. *Multiscale Failure Modelling of Quasi-Brittle Materials*. PhD thesis. Delft University of Technology; 2011.
18. Glüge R, Weber M. Numerical properties of spherical and cubical representative volume elements with different boundary conditions. *Tech Mech*. 2013;33(2):97-103.
19. Hofman P. *Circular Microstructural Volume Elements with Periodic Boundary Conditions for Strain Localization Problems*. MSc thesis. Delft University of Technology; 2021. http://resolver.tudelft.nl/uuid:8c427d42-467f-4baf-a28e-4a4e72acc67c.
20. Crisfield MA, Remmers JJC, Verhoosel CV, De Borst R. *Nonlinear Finite Element Analysis of Solids and Structures*. Wiley; 2012.

How to cite this article: Hofman P, Ke L, van der Meer FP. Circular representative volume elements for strain localization problems. *Int J Numer Methods Eng*. 2022;1-24. doi: 10.1002/nme.7142

10970207, 0, Downloaded from https://onlinelibrary.wiley.com/doi/10.1002/nme.7142 by Tu Delft, Wiley Online Library on [22/11/2022]. See the Terms and Conditions (https://onlinelibrary.wiley.com/terms-and-conditions) on Wiley Online Library for rules of use; OA articles are governed by the applicable Creative Commons License